



## Antarctic isotopic thermometer during a CO<sub>2</sub> forced warming event

Louise C. Sime,<sup>1</sup> Julia C. Tindall,<sup>2</sup> Eric W. Wolff,<sup>1</sup> William M. Connolley,<sup>1</sup> and Paul J. Valdes<sup>2</sup>

Received 9 May 2008; revised 21 July 2008; accepted 24 November 2008; published 31 December 2008.

[1] Results from an isotope-enabled general circulation model are presented in order to determine the isotopic signal of a warmer climate on Antarctica. The warming is forced using CO<sub>2</sub> forecasts for the next century. For unforced interannual climate variability the temporal gradient and correlation between stable water isotopes and surface temperature is small. The relationship is much stronger for the CO<sub>2</sub> forced event. There is little regional coherence between temporal gradients for the forced and unforced climates, implying that correlations between stable water isotopes and temperature from instrumental records of a couple of decades cannot be applied to larger warming events. Additionally, there are strong discrepancies between the forced warming temporal gradients and present-day spatial gradients of isotopes against temperature. We show that it is difficult to obtain a local spatial gradient since it is systematically affected by the geographical size of the spatial sample. For the forced warming, the temporal gradient derived for the warming event over Dome C is less than half the value generally applied. We determine, through means of a new frequency decomposition, that a large portion of this decrease from the expected value is due to changes in the seasonal precipitation temperature covariance. This low isotopic sensitivity to a CO<sub>2</sub> driven warming implies that current and future warming trends may have rather small isotopic signals in Antarctica.

**Citation:** Sime, L. C., J. C. Tindall, E. W. Wolff, W. M. Connolley, and P. J. Valdes (2008), Antarctic isotopic thermometer during a CO<sub>2</sub> forced warming event, *J. Geophys. Res.*, 113, D24119, doi:10.1029/2008JD010395.

### 1. Introduction

[2] The primary control on the spatial distribution of stable heavy water isotopes at high latitudes has been shown to be local temperature [Dansgaard, 1964]. For this reason, the stable water isotopic content of ice cores is used as an indicator of past temperatures. The fractional content of the stable water isotope oxygen-18 is usually expressed as the deviation from a standard water isotope sample, so for H<sub>2</sub><sup>18</sup>O:  $\delta^{18}\text{O} = [1000 \times (^{18}\text{O}/^{16}\text{O})_{V\text{-SMOW}}] - 1$ , with V-SMOW = Vienna standard mean ocean water [e.g., Rozanski *et al.*, 1992]. The method generally applied for central Antarctic ice cores is to substitute the local spatial gradient between surface temperature ( $T_S$ ) and isotopic content  $\delta^{18}\text{O}$  (or equivalently using deuterium  $\delta D$ ) for the expected temporal gradient. This has been used to obtain past temperature records from the isotopic content of Antarctic ice cores including the Vostok [Lorius *et al.*, 1985; Jouzel *et al.*, 1987], EPICA Dome C [EPICA Community Members, 2004; Jouzel *et al.*, 2007] and EDML

(EPICA Dronning Maud Land) ice cores [EPICA Community Members, 2004].

[3] In the vicinity of Vostok, with temperatures between  $-20^\circ\text{C}$  and  $-55^\circ\text{C}$ , a spatial gradient of  $9\text{‰}$   $\delta D$  per  $^\circ\text{C}$  fits the data over a large geographical range [Jouzel *et al.*, 1987; Petit *et al.*, 1999]. Similar geographical spatial gradients apply to the EPICA [EPICA Community Members, 2004] Dronning Maud Land (EDML) and EPICA Dome C [Jouzel *et al.*, 2007] sites. The more recent spatial gradients applied, after making corrections for sea-water isotopic content and altitude change through time, to obtain temperatures from these ice cores have been between  $0.75$  and  $0.82 \text{‰ } ^\circ\text{C}^{-1}$  in  $\delta^{18}\text{O}$  equivalent. Various authors have suggested that there is a 20% uncertainty on these gradients [e.g., Jouzel *et al.*, 2003, 2007; Stenni *et al.*, 2001]. The  $\delta^{18}\text{O}$  equivalent values are obtained by using the factor of 8 difference (due to the average relationship between hydrogen and oxygen isotope ratios) between  $T_S$  against  $\delta D$  and  $T_S$  against  $\delta^{18}\text{O}$  gradients. If these geographically derived gradients do not fit the paleotemperature against isotope record from Antarctic ice cores, this could have implications for our understanding of past temperature changes in Antarctica. Several authors have noted there is not necessarily any causal relationship between the spatial and temporal gradients [e.g., Noone and Simmonds, 2002].

<sup>1</sup>British Antarctic Survey, Cambridge, UK.

<sup>2</sup>School of Geographical Sciences, University of Bristol, Bristol, UK.

[4] The temporal relationship between isotopes and temperature at Antarctic sites can only be directly observed using the short instrumental  $T_S$  and  $\delta^{18}\text{O}$  records. Linear fits to interannual  $T_S$  against  $\delta^{18}\text{O}$  time series show lower gradients and correlations than occur in geographical (spatial) data sets [e.g., Dansgaard *et al.*, 1975; Robin, 1983; Schlosser and Oerter, 2002; Werner and Heimann, 2002; Schmidt *et al.*, 2007]. It is not clear if these weak relationships from short interannual time series are analogous to the larger climatic shifts that the ice cores record [e.g., Jouzel *et al.*, 1994]. Jouzel *et al.* [1997] suggest that stronger “forced” temperature changes increase the  $\delta^{18}\text{O}$  against  $T_S$  gradient.

[5] For Greenland, because of high accumulation rates, it is possible to use inverse models based on borehole thermometry as an independent constraint on the millennial temperature isotope relationship. These, alongside model results, show that precipitation seasonality changes between glacial and interglacial periods reduce the long-term temporal gradient between  $T_S$  and isotopic content to a much lower value than the current spatial gradient [e.g., Cuffey *et al.*, 1995; Hoffmann and Heimann, 1997; Fawcett *et al.*, 1997; Krinner *et al.*, 1997; Werner *et al.*, 2000]. Inland Antarctic core sites borehole thermometry evidence is ambiguous because of rapid signal diffusion due to low precipitation rates [Salamatin *et al.*, 1998]. Additionally, in contrast to Greenland, the Antarctic does not seem to have undergone the same degree of abrupt past temperature changes that Greenland experienced, thus gas isotopic contents ( $^{15}\text{N}/^{14}\text{N}$  and  $^{40}\text{Ar}/^{36}\text{Ar}$ ) have provided only very limited additional paleotemperature evidence [Caillon *et al.*, 2001]. Thus there is no good independent proxy or direct observations of the long-term Antarctic relationship between the stable water isotopes and past temperature.

[6] Jouzel *et al.* [1994] suggested that a good alternative test of temporal gradients is to calculate gradients over a range of climates using an isotopically enabled general circulation model (GCM). For EPICA Dome C, Jouzel *et al.* [2007] show this type of test supports the spatially derived conversion gradient of approximately  $0.75 \pm 0.15\text{‰ } ^\circ\text{C}^{-1}$  in  $\delta^{18}\text{O}$  (see Jouzel *et al.* [2007] supplements). Modeling work by Delaygue *et al.* [2000] and Krinner and Werner [2003] also finds only very limited changes in the seasonality of precipitation between glacial and interglacial times, which supports the use of this gradient. However, Salamatin *et al.* [1998], on the basis of perhaps ambiguous borehole evidence, suggest a temporal slope that might be 50% lower than the local Vostok spatial gradient. Likewise, using different assumptions and again somewhat ambiguous evidence, Caillon *et al.* [2001], Parrenin *et al.* [2001] and Schwander *et al.* [2001] all suggest that the glacial interglacial Antarctic gradient might be 20% lower than the local spatial values.

[7] Here, we use this multiple experiment GCM approach to investigate the isotope-temperature relationship under forced warming conditions. This is attractive for several reasons. Globally warmer time periods are a topic of key current relevance. GCMs are more thoroughly validated for the present day, and the warmer climate conditions we are trying to model are closer to the present day than a glacial climate state. Boundary conditions over a CO<sub>2</sub> driven warming are probably better defined than those for a cold

event. The models have also been more thoroughly investigated for a CO<sub>2</sub> forced warming event, and thus we can have more confidence that the climate processes that change during the warming are better documented, and perhaps understood.

[8] We aim therefore to use these experiments to help fill the gap that exists between our understanding of the short instrumental plus satellite record and the long ice-core record [Schneider *et al.*, 2004]. We set the type of temperature observation that can be obtained from instrumental data (e.g., temperature) in the context of proxy water isotope data [e.g., Petit *et al.*, 1999], and investigate how the proxy should behave under the conditions expected over the next century. This allows us to supplement predictions of temperature change with predictions of changes in precipitation  $\delta^{18}\text{O}$  over the next century and may allow use of the  $\delta^{18}\text{O}$  signal to determine when a significant temperature change has occurred.

[9] We run an isotopically enabled climate model over a CO<sub>2</sub> forced climate warming event. The event is represented by a series of six experiments each with a progressively warmer climate. We use the present-day experiment to examine the spatial distribution of temperature and isotopes, in conjunction with a recently compiled Antarctic isotope database [Masson-Delmotte *et al.*, 2008]. We carry out the analysis using equal area representation of the model output. Additionally we examine the interannual temporal gradients found in the present-day experiment, and compare them to the gradients found over the whole set of warming experiments. To analyze the CO<sub>2</sub> forced warming results, we introduce a new frequency decomposition of the local influences of precipitation and temperature covariance on isotope record of temperature.

## 2. Model and Experiments

[10] The atmospheric model HadAM3 has a regular latitude longitude grid with a horizontal resolution of  $2.5^\circ \times 3.75^\circ$ , and 19 hybrid coordinate levels in the vertical [Pope *et al.*, 2000]. The modeled Antarctic, and global, climatology is similar to that observed [Turner *et al.*, 2006; Pope *et al.*, 2000]. Details of the new stable water isotopic submodel incorporated into HadAM3 that we use here are presented by Tindall *et al.* [2008]. The accuracy of the HadAM3 climatology over Antarctica should enable the isotope output to match observations better than that from some other GCMs since it is generally biases in model climatology which produce the largest errors in modeled isotope output. For example, MUGCM and GENESIS both have significant Antarctic warm biases [Noone and Simmonds, 2002; Mathieu *et al.*, 2002], while GISS has a cold bias [Jouzel *et al.*, 2003]. The Antarctic climate of HadAM3 does seem to be quite close to the later versions of ECHAM [e.g., Hoffmann *et al.*, 1998], which also has quite an accurate simulation of the Antarctic climate.

[11] Approaching the poles, the model grid cell size tends toward zero. This causes problems both with a constant time step (of 30 min) and with the parameterizations used (which are partly grid-size dependent). Therefore to prevent errors and instabilities, due to the Courant-Friedrichs-Lewy criterion, fields are Fourier-filtered near the poles [Pope *et al.*, 2000, and references therein]. This means that cells close to

**Table 1.** Experiment Boundary Conditions

Experiment	SST and Sea Ice	Atmospheric Gas Content		
		CO <sub>2</sub> , ppmv <sup>a</sup>	N <sub>2</sub> O, ppbv <sup>b</sup>	CH <sub>4</sub> , ppmv
PD <sup>c</sup>	HadISST	353	310	1.72
2020 <sup>d</sup>	SRES A1B <sup>c</sup>	410	335	2.2
2040 <sup>d</sup>	SRES A1B <sup>c</sup>	480	352	2.65
2060 <sup>d</sup>	SRES A1B <sup>c</sup>	560	360	2.6
2080 <sup>d</sup>	SRES A1B <sup>c</sup>	630	368	2.3
2100 <sup>d</sup>	SRES A1B <sup>c</sup>	720	370	2.0

<sup>a</sup>Parts per million by volume.

<sup>b</sup>Parts per billion by volume.

<sup>c</sup>Present-day centered on 1990.

<sup>d</sup>Not representing forecast for these absolute dates. See text for further details.

<sup>e</sup>Using sea-ice and sea surface temperature anomalies from the HadCM3 output. See text for further details.

the poles are less independent of each other, although in any GCM there will generally be correlation between nearby grid cells.

## 2.1. Experimental Setup

[12] We present results derived from six experiments: one for the present day (PD) based on 1990, and five between 2020 and 2100 (see Table 1). The PD boundary condition data are based on a monthly average of 1980–1999 HadISST sea surface temperature and sea-ice data. The HadISST data set compares well with other published sea surface temperature analyses [Rayner *et al.*, 2003]. The five future experiments are based on sea surface temperature and sea-ice conditions obtained from the World Climate Research Programme's (WCRP's) Coupled Model Inter-comparison Project phase 3 (CMIP3) runs with HadCM3 [Gordon *et al.*, 2000]. The full ocean and atmosphere Special Report on Emissions Scenarios (SRES) A1B HadCM3 experiment provide a good basis for the future experiment boundary conditions: the run is well-documented and consistent with our isotope enabled HadAM3 model.

[13] The A1B future scenario is not necessarily considered more likely than any of the other CMIP3 future scenarios. In

terms of global temperature, it is about the middle of the range of changes projected by the different CMIP3 scenarios and suggests a centennial warming of  $\sim 3^{\circ}\text{C}$  [Bracegirdle *et al.*, 2008]. The run scenario ends at the year 2100 which constrains the forcing period for the isotope enabled HadAM3 experiments. Note that as Table 1 shows, although the warming is driven by a mixture of greenhouse gases (GHG), here we use CO<sub>2</sub> and GHG driven warming interchangeably; that is, where CO<sub>2</sub> is written, we wish to imply CO<sub>2</sub> equivalent GHG forcing.

[14] The HadCM3 SRES A1B sea surface temperature output has some regional biases compared with the PD HadISST sea surface temperature. These biases can affect the modeled Antarctic climatology. For example, tropical warm sea surface temperature biases in HadCM3 over Indonesia and the eastern tropical Atlantic cause mean sea level pressure errors around Antarctica [Lachlan-Cope and Connolley, 2006]. The effect of these sea surface temperature model biases is minimized by applying the HadCM3 SRES A1B sea surface temperature fields as anomalies to the HadISST sea surface temperature boundary conditions [e.g., Krinner *et al.*, 2008]. Use of 10-year average HadCM3 SRES A1B sea surface temperatures avoids interannual run variability affecting the experiments. As an example, the 2080 experiment sea surface temperature field is formed by subtracting a 10-year monthly mean of 2000 to 2010 from a 10-year monthly mean of 2070 to 2080 and then adding the resultant anomaly to the present-day HadISST sea surface temperature.

[15] The use of the anomalies, while minimizing HadCM3 error bias, means that the 2020 is effectively separated by a smaller warming anomaly than would be expected (effectively 10 years) from the present-day run. Beyond 2020, the experiments are each separated by 20-year anomalies. As a result, the set of runs is indicative of anomalous SRES A1B warming over a 90-year rather than 100-year SRES A1B scenario HadCM3 run. Use of anomalies displaces any possible absolute dates of the future experiment. However, for the purposes of this investigation we only wish to model

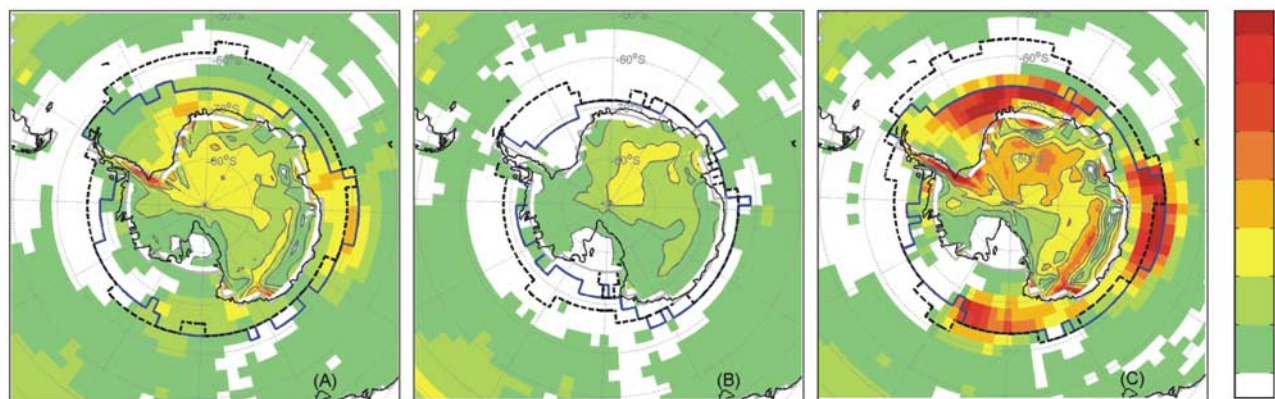


**Figure 1.** Shading shows the surface temperature difference between experiments 2100 and PD (see Table 1) for (a) annual, (b) summer, and (c) winter conditions. Blue solid lines show the 25% ice concentration boundaries for 2100 and dashed black lines are for present day. Outside Antarctica the shading is sea surface temperature difference (forcing applied to the atmospheric model). Inside Antarctica the shading is surface temperature difference, i.e., the response to the atmospheric gas forcing and to the sea surface temperature and sea ice, themselves dependent on atmospheric gas forcing.

a plausible magnitude CO<sub>2</sub> warming signal: “absolute” dates are not meaningful or of interest and have no effect on the findings presented.

[16] After the sea surface temperature anomalies are applied, any resulting sea surface temperatures of less than  $-1.8^{\circ}\text{C}$  are set to  $-1.8^{\circ}\text{C}$  to avoid improbably low values

(as done by *Paul and Schäfer-Neth* [2003]). We do not use sea-ice anomalies since negative sea ice occurs. Therefore sea-ice conditions from the HadISST data set are used for the present-day experiment then from the SRES A1B HadCM3 data set for the 2020 to 2100 experiments. Figure 1 shows the mean annual anomalous sea surface temperatures and the sea-ice conditions at 2100 for mean annual, summer (DJF) and winter (JJA) seasons. The change between experiments PD to 2100 in sea surface temperature is relatively linear, so the 2020 to 2080 experiments are similar to scaled versions of the 2100 anomalies shown.

[17] For the 2100 experiment the annual average sea surface temperature anomalies at  $50^{\circ}\text{S}$  are  $1.3$  to  $1.5^{\circ}\text{C}$  warmer in a nearly zonally constant pattern with a limited seasonal signature. South of  $50^{\circ}\text{S}$  the sea surface temperature anomaly become more strongly seasonal and zonally dependent. At  $70^{\circ}\text{S}$  the zonally averaged annual mean anomaly is  $2.3^{\circ}\text{C}$  with a seasonal spread of  $3^{\circ}\text{C}$  (zonal mean anomaly in summer of  $0.5^{\circ}\text{C}$  and winter of  $3.5^{\circ}\text{C}$ ). Sea-ice loss is at a maximum at  $70^{\circ}\text{S}$  with approximately 25% losses in fractional cover for the annual average. The maximum losses in summer are farther south at  $72.5^{\circ}\text{S}$  and slightly northward at  $67.5^{\circ}\text{S}$  in winter.

[18] The surface ocean  $\delta^{18}\text{O}$  value used for all experiments is uniformly zero. Over polar regions, initial test experiments (not shown here) using the current global ocean (and lake) surface distribution of  $\delta^{18}\text{O}$  produced  $\delta^{18}\text{O}$  in precipitation results that were almost identical to those from uniform source condition experiments. Using an atmosphere only model means that we cannot simulate the oceanic and lake warmer experiment distribution of  $\delta^{18}\text{O}$ . The limited polar differences in  $\delta^{18}\text{O}$  in precipitation simulated by using the observed oceanic and lake distribution of  $\delta^{18}\text{O}$  leads us to believe that the  $\delta^{18}\text{O}$  in precipitation (for the warming event simulated here) will not be sensitive to realistic changes in this boundary condition. Thus our constant and uniform surface ocean  $\delta^{18}\text{O}$  seems a reasonable approach.

## 2.2. Present-Day Climate

### 2.2.1. Precipitation

[19] The match between HadCM3 modeled and observed Antarctic climatology is closer than for most other GCMs [*Bracegirdle et al.*, 2008]. Even using HadAM3 (which is HadAM3 coupled to an ocean GCM), which is known to have incorrect sea level pressure around Antarctica due to tropical sea surface temperature errors, the atmospheric model rates amongst the top few models (fourth of 19 of the IPCC AR4 models) for its atmospheric representation of the Antarctic [*Connolley and Bracegirdle*, 2007]. Additionally

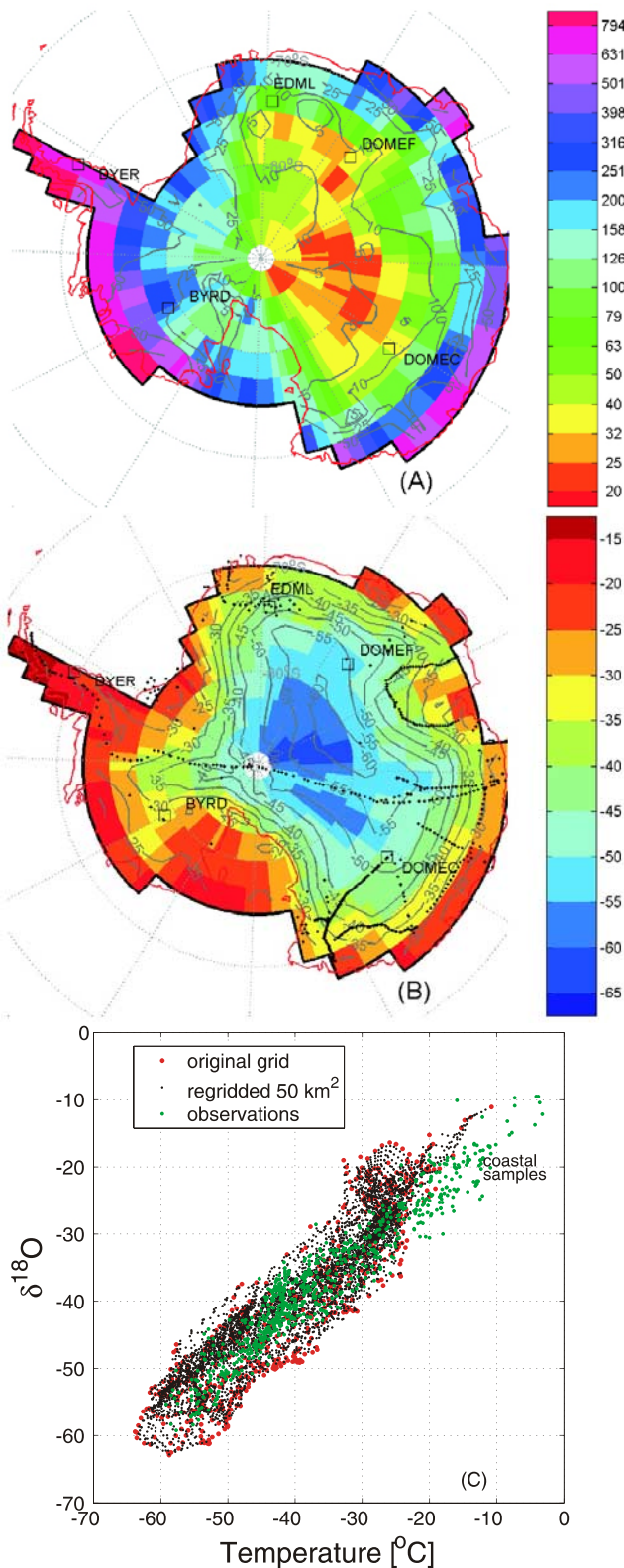


**Figure 2.** (a) Shading shows mean PD (20 year) precipitation ( $\text{kg m}^{-2} \text{a}^{-1}$  equal to  $\text{mm a}^{-1}$  water equivalent) on a logarithmic color scale, contours show the increase in precipitation that occurs between the PD and 2100 experiments (using approximately logarithmic contour intervals). (b) Shading shows mean PD (20 year) experiment  $\delta^{18}\text{O}$  and the  $5^{\circ}\text{C}$  contours for PD  $T_{\text{S}}$ . Black dots show location of the *Masson-Delmotte et al.* [2008] observations. (c) Scatterplots of  $\delta^{18}\text{O}$  against  $T_{\text{S}}$  for the natural model grid in red, the equal area grid (see text) in black, and the *Masson-Delmotte et al.* [2008] observations in green.

we note that without the tropical sea surface temperature errors, eliminated here by the use of the HadISST sea surface temperature data, the simulation is more accurate [e.g., *Krinner et al.*, 2008]. The geographical distribution of the modeled precipitation (Figure 2a) minus evaporation and temperature compares quite favorably both with observations, and with ECMWF output for the majority of the continent [*Turner et al.*, 2006].

[20] Mean Antarctic precipitation for the present-day run is  $182.8 \text{ kg m}^{-2} \text{ a}^{-1}$  (Figure 2a); sublimation is  $13.1 \text{ kg m}^{-2} \text{ a}^{-1}$ , giving a total mean accumulation rate of  $169.7 \text{ kg m}^{-2} \text{ a}^{-1}$ . This compares to mean accumulation estimates of  $143 \pm 4 \text{ kg m}^{-2} \text{ a}^{-1}$  [*Arthern et al.*, 2006];  $151 \text{ kg m}^{-2} \text{ a}^{-1}$  [*Turner et al.*, 1999]; and  $182 \text{ kg m}^{-2} \text{ a}^{-1}$  [*Monaghan et al.*, 2006]. We note that the modeled values could be slightly inflated owing to the model land masking. High-accumulation regions such as the Ross Sea Embayment and the Peninsula region are represented by regions which are too large (e.g., see difference between true coast and modeled coastline in Figure 2). However, the modeled accumulation values are still within the range of observationally derived estimates.

[21] The present-day experiment has a low-amplitude seasonal precipitation signal. There is only rather limited observational information on the inland Antarctic seasonal cycle [e.g., *Bromwich*, 1988; *Ekaykin et al.*, 2002] with which we can compare the modeled precipitation seasonality. *Bromwich* [1988] suggested that most precipitation in East Antarctic may fall in winter, despite the low average moisture content of the air, owing to more intense winter cyclones activity. However, *Marshall* [2008] suggests in total the evidence is somewhat equivocal with some of the records referenced by *Bromwich* [1988] indicating a slight winter maximum (for Vostok [1988] indicating a semi-annual pattern for South Pole). The modeled present-day run has an East Antarctic (see Figure 3 for regional definitions) summer precipitation maximum peaking in December at 11% above the mean annual precipitation value. This is supported by the recent *Fujita and Abe* [2006] East Antarctic record for Dome F which also indicates a summer maximum. By 2100, the modeled East Antarctic summer maximum has reduced to +7% in December and the cycle has become flatter with a semiannual pattern featuring a second +7% peak in May (spatial pattern of increase between PD and 2100 shown by contouring on Figure 2a). For the rest of the continent, there is a winter maximum in modeled present day precipitation: +17% from May till August for the West Antarctic; +22% for the Peninsula, with a hint of a semiannual cycle; and the average for the whole continent is +15% between April and June. For regions with a winter maxima in precipitation the 2100 cycle amplitude is larger than that for the present day with the regions all increasing by about 10%. We also note a substantial increase in the annual mean precipitation total for all regions over the warming event of between 15 and 20%.

### 2.2.2. Temperature and $\delta^{18}\text{O}$ in Precipitation

[22] The isotopic results from HadAM3 enable us to examine in detail the relationship between stable water isotope values and temperature. In this case we do this specifically within the context of a warming world. Although we note that the deuterium excess can provide

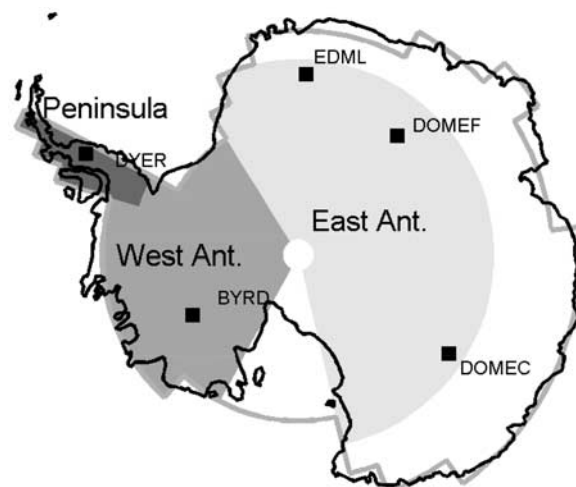


**Figure 3.** Schematic showing the definition of model regions discussed in the text.

useful isotope derived climate insight [e.g., *Masson-Delmotte et al.*, 2008], herein, we confine our analysis to the oxygen-18 isotope results.

[23] Figures 2b and 2c show the modeled present-day pattern of surface temperature and  $\delta^{18}\text{O}$ . The largest absolute errors in the mean annual PD experiment surface temperature  $T_S$  are in the Dronning Maud land close to  $80^\circ\text{S}$ ,  $20^\circ\text{W}$  and near  $45^\circ\text{E}$ , where the orography is too high and too low, respectively. Additionally the highest points of East Antarctic do not reach more than 4000 m, and the coastal and Peninsula regions have topographic slopes which are too low (not shown). Thus the extremes of both coastal slopes and high plateaus are not fully represented by the model. This is due to the relatively coarse resolution of the model grid. Errors in orography also produce the largest temperature errors in comparable isotopically enable GCMs [*Hoffmann et al.*, 1998; *Mathieu et al.*, 2002]. Apart from the orographically induced errors, the mean annual PD experiment  $T_S$  compares quite well with in situ estimates. *Turner et al.* [2006] note that the low-temperature inversion is up to  $5^\circ\text{C}$  too strong in the central interior. Apart from this region, the basic inversion pattern and strength generally matches the best observations within a few percent. But comparative inversion observations are rather sparse and may themselves not be representative [*Conolley*, 1996].

[24] In terms of absolute Antarctic  $T_S$  (surface temperature) and  $\delta^{18}\text{O}$  values the PD run compares well with the *Masson-Delmotte et al.* [2008] database (see Figure 2c). (See *Tindall et al.* [2008] for the global modeled distribution of  $T_S$  and  $\delta^{18}\text{O}$  values compared to observations.) The lack of the coldest temperatures and most depleted  $\delta^{18}\text{O}$  values in the observations seems to reflect the distribution of the observations with none in the *Masson-Delmotte et al.* [2008] database for the coldest Dome A region around  $85^\circ\text{S}$   $70^\circ\text{E}$  (see Figure 2b). The absence of the warmest  $T_S$  and least depleted  $\delta^{18}\text{O}$  values on the model grid is partly due to the relatively coarse grid resolution at the coast; the highest  $T_S$  model sites represent averaged areas farther inland than the observations. The maximum  $T_S$  in the regridded data is sensitive to whether we interpolate using

marine temperature values or use only continental grid cells. If we regrid including marine temperatures, the maximum  $T_S$  is higher. Using marine grid cells can also bring the modeled  $\delta^{18}\text{O}$  range into closer agreement with the *Masson-Delmotte et al.* [2008] database. However, here we use a more conservative approach and do not interpolate any values beyond the natural grid continental edge midpoint of the cells. We do the same for the most southerly cells, meaning we lack values for the most poleward and most coastal parts of the continent.

### 2.3. Forced Warming

[25] The total mean Antarctic warming of 2.6°C over the experiment set lies quite centrally in the range of the *Intergovernmental Panel on Climate Change* [2007] CMIP3 SRES A1B output [Bracegirdle et al., 2008]. While different models disagree in detail on the Antarctic climatological changes throughout the A1B scenario [Bracegirdle et al., 2008], this set of experiments provides a basis for assessing the isotope-temperature relationship over a meaningful CO<sub>2</sub> forced warming. The warming rate is very similar to the total global warming of 2.7°C although total Southern Hemisphere warming is 1.9°C (Northern Hemisphere is 3.5°C), owing to the slow rate of warming in response to greenhouse gas increase in the Southern Ocean [Manabe et al., 1991] (see Figure 1). Sea-ice changes are important, particularly in the coastal regions [Bracegirdle et al., 2008].

[26] In Antarctica, recent change has been small over most of the continent [Schneider et al., 2006; Monaghan et al., 2006], but very significant warming has been observed in the Antarctic Peninsula region [Vaughan et al., 2003], and this has been associated with the loss of a number of ice shelves. We attempt to elucidate how the different regions will respond by defining four different Antarctic regions, shown in Figure 3 (the fourth region not labeled on Figure 3 is the whole of the Antarctic), and examine the temperature changes and isotope changes within them individually. Additionally, we look at the isotope response to temperature change at five core sites.

[27] The Peninsula shows the strongest warming until 2080, probably owing to the greater influence of sea-ice losses on the warming rate [e.g., Bracegirdle et al., 2008]. The East Antarctic shows linear warming after a slight cooling in 2020. By 2100 the warming is of similar magnitude to that in the Peninsula region. The West Antarctic shows quite linear warming, i.e., quicker initially than in the East Antarctic, then a rate slower than the East Antarctic over 2060 to 2100. By 2100 the West Antarctic is slightly less warmed compared to the East Antarctic. See Figure 1 for overall warming. These trends are amplified in the winter mean  $T_S$ . Summer trends are all more linear. By 2100 the annual mean  $T_S$  anomaly of the Peninsula is +2.9°C; the East Antarctic +3.0°C; the West Antarctic is +2.4°C. Most of the warming takes place in winter: the whole Antarctic is +3.4°C; the Peninsula is +3.7°C; the East Antarctic +3.9°C; the West Antarctic is +2.9°C whereas in summer the whole Antarctic is +1.8°C; the Peninsula is +1.4°C; the East Antarctic +2.7°C; the West Antarctic is +1.9°C. The autumn and spring pattern of warming south of 50°S is strongly zonally and seasonally dependent. After 2020 all the experiments show relatively linear warming in all seasons and in the mean average. But we note that the 2020 results are slightly anomalous in their

seasonality, compared with the PD and the later experiments. This appears to reflect changes in the sea ice since PD uses observed sea ice while 2020 and beyond use HadCM3 sea ice. But generally, all experiments from 2040 onward and all regions show a weak summer warming and a stronger winter warming.

### 3. Using $\delta^{18}\text{O}$ as a Proxy for Temperature

[28] To use  $\delta^{18}\text{O}$  as a proxy for spatial or temporal temperature, it is the general convention to define a gradient as the linear relationship  $\delta^{18}\text{O} = a_S T_S + b$  so that  $a_S = \Delta\delta^{18}\text{O}/\Delta T_S$ , where  $T_S$  is the surface temperature. This relationship can be applied to sets of spatial or temporal  $\delta^{18}\text{O}$  and  $T_S$  observations to obtain either spatial  $a_S^{\text{SPACE}}$  or temporal  $a_S^{\text{TIME}}$  gradients. We use the least squares fit method since it provides a straightforward means to obtain linear regression fit statistics and gradients for the  $\delta^{18}\text{O}$  against  $T_S$  relationship.

[29] Since  $\delta^{18}\text{O}$  is recorded in precipitation, and is therefore already “precipitation-weighted” we also compare  $\delta^{18}\text{O}$  with a precipitation-weighted version of the surface temperature for each longitudinal and latitudinal position  $(x, y)$  calculated,

$$T_{SPt}(x, y) = \frac{\sum_t (T_S(x, y) P_t(x, y))}{\sum_t P_t(x, y)}, \quad (1)$$

where  $t$  is increments of time (herein  $t$  is daily, so that  $t = 1..365$ ) and  $P$  is precipitation.

[30] Warmer air tends to be associated with higher absolute humidity so that warm air masses can contribute more precipitation. Additionally cloud cover will tend to reduce radiative cooling [e.g., Kohn and Welker, 2005]. So changes in  $T_{SPt}$  may tend to be smaller than changes in  $T_S$ . Werner and Heimann [2002] have shown that in some instances  $T_{SPt}$  can deviate significantly from  $T_S$ . Understanding these differences is essential to fully comprehending how changes in  $T_{SPt}$  relate to changes in  $T_S$  and thus how  $\delta^{18}\text{O}$  relates to  $T_S$ . We call this difference “biasing”  $B$  so

$$B(x, y) = T_{SPt}(x, y) - T_S(x, y). \quad (2)$$

[31] Variations in  $B$  (with space and/or climate) causes differences between the spatial and temporal gradients calculated using  $T_S$  and those that would be obtained using an equivalent precipitation derived ice-core record. It is useful therefore to define (as above) gradients between  $\delta^{18}\text{O}$  and  $T_{SPt}$ . We term the new spatial and temporal gradients of  $\delta^{18}\text{O}$  against  $T_{SPt}$ :  $a_{SPt}^{\text{SPACE}}$  and  $a_{SPt}^{\text{TIME}}$ , respectively. Therefore  $a_{SPt}^{\text{SPACE}}$  and  $a_{SPt}^{\text{TIME}}$  are versions of  $a_S^{\text{SPACE}}$  and  $a_S^{\text{TIME}}$  using precipitation-weighted temperature.

#### 3.1. Spatial Gradients of $\delta^{18}\text{O}$ Against $T_S$ and $T_{SPt}$

[32] Spatial gradients  $a_S^{\text{SPACE}}$  and  $a_{SPt}^{\text{SPACE}}$  are presented in Table 2 for the regions shown in Figure 3, and for the whole of the Antarctic. Using standard model latitude longitude gridded output it is not simple, near the poles, to calculate the uncertainty associated with spatial relationships between  $\delta^{18}\text{O}$  and temperature. Adjacent spatial data points cannot be fully independent within a GCM output, or an observation set, because there is correlation between nearby points. But this problem is exacerbated approaching the poles,

**Table 2.** Spatial Gradients  $a_S^{SPACE}$  and  $a_{SPt}^{SPACE}$ , Using Mean From 20-Year Experiments<sup>a</sup>

Region or Core Site	Using Unweighted $T_S$			Using P-Weighted $T_{SP}$		
	$a$	CI <sub>95</sub>	EV	$a$	CI <sub>95</sub>	EV
<i>20-Year Means of the PD Run<sup>b</sup></i>						
Antarctic	0.89	±0.04	0.89	0.96	±0.04	0.90
East Antarctic	0.73	±0.08	0.77	0.72	±0.08	0.77
West Antarctic	1.28	±0.19	0.77	1.23	±0.16	0.81
Peninsula	0.62	±0.24	0.84	0.80	±0.31	0.84
<i>Summer Values DJF<sup>b</sup></i>						
Antarctic	1.03	±0.03	0.93	1.08	±0.04	0.92
<i>Winter Values JJA<sup>b</sup></i>						
Antarctic	0.90	±0.04	0.86	0.85	±0.04	0.88
<i>20-Year Means of the 2100 Run<sup>b</sup></i>						
Antarctic	0.91	±0.04	0.90	0.99	±0.04	0.90
East Antarctic	0.72	±0.07	0.79	0.73	±0.08	0.78
West Antarctic	1.37	±0.18	0.81	1.28	±0.16	0.83
Peninsula	0.68	±0.25	0.86	0.86	±0.26	0.89
<i>PD Radius of 300 km (~112 × 50 km<sup>2</sup>)<sup>c</sup></i>						
DOMEC	1.36	±0.66	0.91	0.99	±0.70	0.82
EDML	0.67	±0.21	0.96	0.72	±0.33	0.91
DOMEF	0.70	±0.37	0.89	0.78	±0.51	0.84
BYRD	1.28	±1.16	0.75	1.04	±0.59	0.88
DYER	0.56	±0.42	0.78	0.94	±0.38	0.93
<i>PD Radius of 500 km (~314 × 50 km<sup>2</sup>)</i>						
DOMEC	0.94	±0.29	0.78	0.79	±0.24	0.79
EDML	0.66	±0.08	0.96	0.71	±0.14	0.89
DOMEF	0.69	±0.18	0.82	0.66	±0.28	0.65
BYRD	1.18	±0.34	0.80	1.12	±0.23	0.89
DYER	0.51	±0.13	0.84	0.79	±0.15	0.90
<i>2100 Radius of 500 km (~314 × 50 km<sup>2</sup>)</i>						
DOMEC	0.96	±0.28	0.81	0.82	±0.20	0.85
EDML	0.71	±0.07	0.97	0.74	±0.11	0.94
DOMEF	0.66	±0.19	0.81	0.68	±0.28	0.67
BYRD	1.18	±0.33	0.81	1.13	±0.24	0.88
DYER	0.48	±0.13	0.82	0.73	±0.15	0.88

<sup>a</sup>Notation:  $a$ , gradient; CI<sub>95</sub>, mean 95% confidence interval for  $a$ , assuming model grid point independent at 65°S (see text); EV, explained variance ( $R^2$ ).

<sup>b</sup>Using 20-year means of the PD or 2100 experiment as marked; see Table 1.

<sup>c</sup>The degrees of freedom calculated for this sampling radius are about 15. Any geographical sampling radii less than 300 km gives an insufficient amount of independent locations (too few degrees of freedom in the model output) to obtain a meaningful linear fit.

because the degree of independence decreases with the grid cell size (which is partly why the model uses Fourier filtering near the poles to decrease the model degrees of freedom approximately in proportion with an equal area representation). To counteract these problems of latitudinally dependent grid autocorrelation affecting results, particularly in the calculation of uncertainties, and to allow a better comparison with available data, we regrid the model output to an equal area grid. Equal area regridding onto a 50-km grid gives 20 points to represent a natural model grid point at 65°. This linearly decreases to 12 points at 75°S (at Dome C) and 0 at the poles. We regrid using a linear two-dimensional interpolation model. Note that if an appropriately rotated grid was used, to provide a polar grid which was approximately equal area, this regridding would be unnecessary.

[33] The equal area regridded model results are used to obtain  $a_S^{SPACE}$  and  $a_{SPt}^{SPACE}$ . Even using equal area output, it is not clear how to objectively estimate the degrees of freedom

in each spatial data set. Here as a simple approximation to the true degrees of freedom we assume the natural model grid points at 65°S are independent. This means that for the 50 km<sup>2</sup> equal area grid version each set of 20 adjacent data points represent one degree of freedom. We use this consistently throughout the spatial gradient analysis. While this is still not correct, because the cells at 65°S will be partially spatially correlated, 65°S is generally out with the region of model Fourier filtering and the approach at least gives a consistent approach to estimating the uncertainties.

[34] The values of  $a_S^{SPACE}$  shown in Table 2 are similar to the published spatial gradient from observations. *Masson-Delmotte et al.* [2008] collate the most complete database of surface Antarctic snow isotopic composition and use the data set to calculate spatial gradients. Their  $\delta^{18}\text{O}$  gradient for the entire new Antarctic spatial database is  $a_S^{SPACE} = 0.80 \pm 0.01\text{‰ } ^\circ\text{C}^{-1}$ . This is  $0.09 \pm 0.05\text{‰ } ^\circ\text{C}^{-1}$  lower than the modeled present-day value in Table 2. We note that the PD model value of  $a_S^{SPACE} = 0.89 \pm 0.04\text{‰ } ^\circ\text{C}^{-1}$  is also higher than previous observation-based estimates of  $\delta^{18}\text{O}$   $a_S^{SPACE}$  that were around  $0.75\text{‰ } ^\circ\text{C}^{-1}$  [e.g., *Lorius and Merlivat*, 1977; *Jouzel et al.*, 2003, and references therein].

[35] The *Masson-Delmotte et al.* [2008] database is not evenly geographically distributed across Antarctica. More than 82% of the observations are located in the East Antarctic region, and there mostly in the sector from 90°E to 180°E. However, our East Antarctic gradient is  $0.73 \pm 0.08$  which matches the observed gradient for the best comparable data in the *Masson-Delmotte et al.* [2008] observation set. Additionally, we note that our two modeled values (Antarctic and East Antarctic) of  $a_S^{SPACE}$  enclose the observational based estimate of  $a_S^{SPACE}$ , and the observation geographical sampling seems to fall somewhere between our definition of an evenly sampled Antarctic and our East Antarctic. Thus the discrepancy between the modeled and observational estimate of  $a_S^{SPACE}$  appears to be at least as likely due to the uneven geographical sampling of the observations as to inaccuracy, or resolution-dependent imprecision, in the model output. The difference between the  $0.75\text{‰ } ^\circ\text{C}^{-1}$  *Lorius and Merlivat* [1977] estimate and the  $0.80 \pm 0.01\text{‰ } ^\circ\text{C}^{-1}$  *Masson-Delmotte et al.* [2008] gradients are also likely to be due to the differing geographic samples.

[36] *Masson-Delmotte et al.* [2008] examine the geographic pattern of local spatial gradients by calculating  $a_S^{SPACE}$  using multiple local subsets of  $\delta^{18}\text{O}$  and  $T_S$  observations. Each subset of values is selected according to whether it lies within a set distance from the location of interest. We follow the same methodology here to examine the variation of  $a_S^{SPACE}$  across Antarctica for the experiments. Figure 4 shows the results of  $a_S^{SPACE}$  fits for the PD experiment using fits based on sampling radii as noted. We also calculate values of  $a_{SPt}^{SPACE}$ . These are generally slightly higher than  $a_S^{SPACE}$ , but the spatial pattern is very similar so is not shown.

[37] Figure 4 shows clear geographical structure in  $a_S^{SPACE}$  (repeated in  $a_{SPt}^{SPACE}$ , not shown). The general geographical pattern is similar to that shown by *Helsen et al.* [2007] obtained using a backward trajectory isotope model, suggesting that the pattern obtained is robust between different types of model. Likewise using sampling radii similar to those used by *Masson-Delmotte et al.* [2008] the

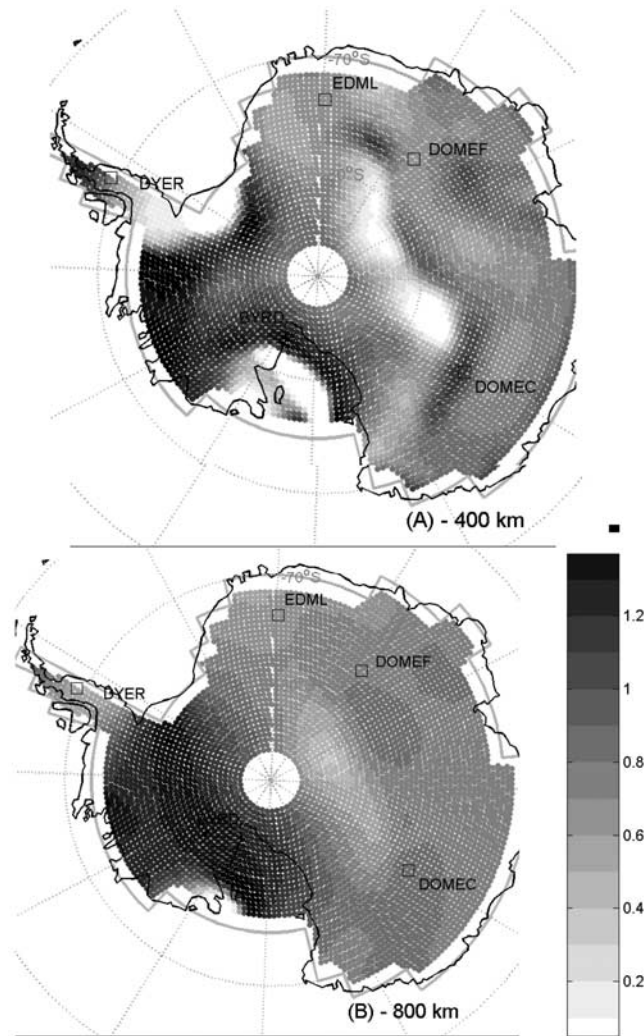


**Figure 4.** Spatial gradients  $a_S^{SPACE}$  (the gradient of  $\delta^{18}O$  against  $T_S$  over local regions) for the PD using least squares fits using (a) 400-km and (b) 800-km sampling radii.

geographical structure of  $a_S^{SPACE}$  seems to compare both quantitatively and qualitatively quite well to that from the observations. For example both observation and model results show low gradients in central regions; locally around Vostok  $a_S^{SPACE}$  can be less than  $0.2\text{‰ }^\circ\text{C}^{-1}$ . Additionally, both show a strong southward decrease in  $a_S^{SPACE}$  along the Peninsula and high  $a_S^{SPACE}$  values in the Weddell Sea embayment. The sparse nature of the observations make a more detailed comparison difficult.

[38] Precipitation-weighted gradients  $a_{SPt}^{SPACE}$  tend to be a little higher than  $a_S^{SPACE}$  (on average about  $+0.02\text{‰ }^\circ\text{C}^{-1}$ ). The largest difference between  $a_S^{SPACE}$  and  $a_{SPt}^{SPACE}$  occurs in the Peninsula region. This is due to the large meridional gradient in  $B$  over this area, with small  $B$  at the northern tip and larger  $B$  values inland (not shown here). This  $B$  correlates with  $T_S$  so that  $a_{SPt}^{SPACE}$  is larger than  $a_S^{SPACE}$  since, for the colder southerly Peninsula portions, the reduction in  $T_{SPt}$  is lower than the reduction in  $T_S$ . Thus the spatial reduction in  $\delta^{18}O$  is applied over a lesser reduction in  $T_{SPt}$  than  $T_S$ , leading to a higher  $a_{SPt}^{SPACE}$  value. In general, any

regions with a spatial correlation between  $B$  and  $T_S$  are liable to produce differences between  $a_S^{SPACE}$  and  $a_{SPt}^{SPACE}$ . The other regions show relatively small changes between  $a_S^{SPACE}$  and  $a_{SPt}^{SPACE}$  because there is a less systematic relationship between  $B$  and  $T_S$  (and  $\delta^{18}O$ ).

[39] Interestingly, we find a strong dependence of  $a_S^{SPACE}$  (and  $a_{SPt}^{SPACE}$ ) on the applied subset sampling radius. This is illustrated by the change between Figures 4a and 4b, and is clarified in Figure 5a. The mean Antarctic values of  $a_S^{SPACE}$  and  $a_{SPt}^{SPACE}$  increase strongly with the spatial sampling radius used to define the local data subset. Likewise the mean correlations obtained for the linear fits are also related to the spatial radius (Figure 5b). This implies that it is difficult to obtain a local spatial gradient, since it is clearly strongly systematically dependent on the subset sampling radius used. This indicates that a serious problem may occur if we try to define a “representative” local  $a_S^{SPACE}$  value.

[40] Table 2 also shows core site results for  $a_S^{SPACE}$  for 2100. None of the gradients calculated are significantly different between the experiments, although there does seem to be slight tendency for the 2100  $a_S^{SPACE}$  values to be higher than those for PD. However, in general the model

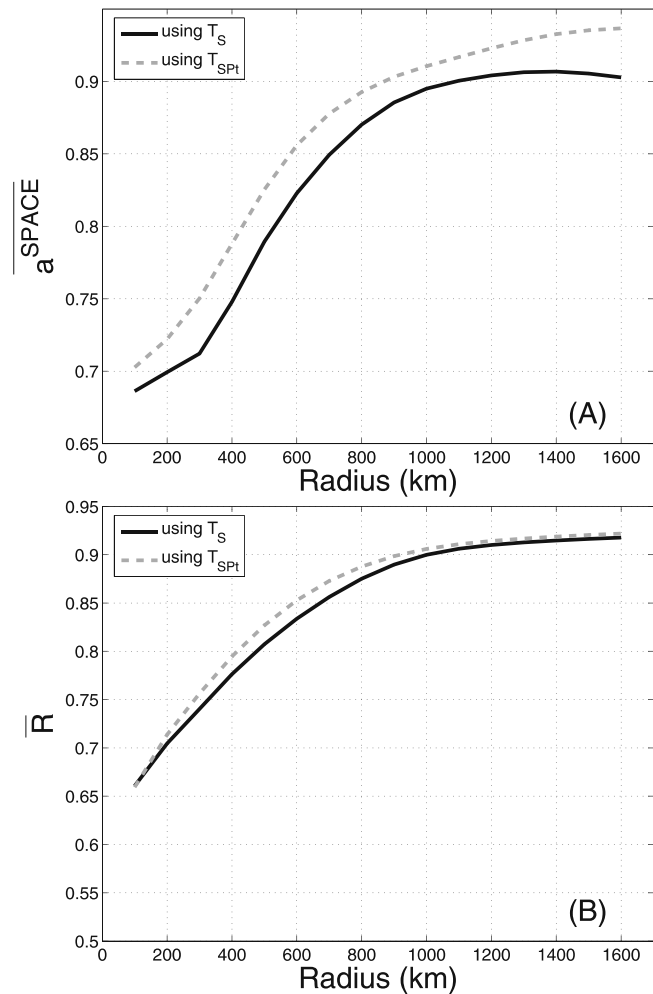


**Figure 5.** (a) Mean of all the spatial gradients over all Antarctic locations ( $a_{SP}^{SPACE}$ ) against the spatial sampling radius and (b) the mean Antarctic correlations ( $\bar{R}$ ) associated with the same fits.

**Table 3.** Temporal Gradients  $UFa_S^{TIME}$  and  $UFa_{SPt}^{TIME}$ , Using Interannual PD Experiment (Unforced)<sup>a</sup>

Region	Using Unweighted $T_S$			Using P-Weighted $T_{SPt}$		
	$a$	CI <sub>95</sub>	EV	$a$	CI <sub>95</sub>	EV
Antarctic	0.17	±0.37	0.05	0.34	±0.30	0.25
East Antarctic	0.18	±0.42	0.05	0.47	±0.26	0.45
West Antarctic	0.16	±0.60	0.02	0.20	±0.28	0.11
Peninsula	0.39	±0.30	0.29	0.50	±0.22	0.56

<sup>a</sup>Notation:  $a$ , gradient; CI<sub>95</sub>, mean 95percent; confidence interval for  $a$ ; EV, explained variance ( $R^2$ ). Unforced fits are from 20 years of mean annuals, using annual means averaged across each region for each of the 20 years of the PD experiment.

results suggest the observed stability of the spatial slope in the Dome C region over 20 years [Masson-Delmotte *et al.*, 2008] remains relatively unchanged (over the majority of the continent) over this CO<sub>2</sub> forced warming event.

### 3.2. Unforced Interannual Temporal Gradients

[41] One of the interesting questions in the literature is whether there really is a difference between the values of  $a_S^{TIME}$  calculated using the short records of temperatures and isotopes over a decade or two where no forced change is applied [e.g., Schlosser and Oerter, 2002; Werner and Heimann, 2002], and those from situations where forced centennial or millennial climate change occurs [e.g., Jouzel *et al.*, 1997]. To examine this we present (unforced, UF)  $UFa_S^{TIME}$  calculated from PD experiment mean annual values over a 20 year run (Table 3), and compare these to (forced, F)  $Fa_S^{TIME}$  calculated over the 2.6°C forced warming event charted by the 6 experiments (see Table 1) and shown in Table 4.

[42] The results for the  $UFa_S^{TIME}$  and  $UFa_{SPt}^{TIME}$  are calculated using the unforced mean annual values for the 20-year present-day run. As in section 3.1 we use the equal area gridded results for the linear least square fitting. In most cases we do some spatial averaging prior to the fitting. This is indicated in each case, as in the previous section, by a spatial sampling radius. Using the same grid and equivalent sampling procedures helps to make the temporal gradient calculated directly comparable to the spatial gradients.

[43] The linear fit gradients are shown in top of Table 3 and by Figure 6. As observed by Schlosser and Oerter [2002] and modeled by Hoffmann *et al.* [1998] and Werner and Heimann [2002] the regionally averaged unforced PD temporal fits have low explained variances. The linear fits show that  $T_S$  generally accounts for less than 10% of the variance in  $\delta^{18}O$  except in the Peninsula region where the explained variance rises to 30%. Figures 6a and 6b show that the spatial pattern of  $UFa_S^{TIME}$  is variable with the possibility of better correlations and higher gradients in local, mainly coastal, locations. We have not ascertained here what determines these locations. Note that these short-term (20-year) time series are from simulations run with climatological mean SST and sea ice. This reduces the model degrees of freedom owing to remote large-scale interannual variability (described by, e.g., Schneider and Noone [2007] which is liable to reduce our modeled interannual correlations and gradients between  $\delta^{18}O$  and  $T_S$  compared to the observations and the coupled interannual relationships modeled by Schmidt *et al.* [2007].

[44] As Schlosser and Oerter [2002] note from observations at Neumayer, the correlation coefficients for  $UFa_{SPt}^{TIME}$  using the precipitation-weighted temperature are considerably higher than those found with  $UFa_S^{TIME}$  (differences between top and bottom panels on Figure 6), as are the gradients themselves. The Antarctic average for  $UFa_S^{TIME}$  is 0.20‰ °C<sup>-1</sup>, and for  $UFa_{SPt}^{TIME}$  it increases to 0.42‰ °C<sup>-1</sup>. Thus it seems that as Schlosser and Oerter [2002] suggest, a large degree of  $\delta^{18}O$  variance unexplained by  $UFa_S^{TIME}$  may relate to interannual variability in seasonality, or other local parameters. This shows that  $T_S$  is not very well correlated with  $T_{SPt}$  for these interannual temperature values. The coefficients of correlation contoured on Figures 6c and 6d also show that even using  $UFa_{SPt}^{TIME}$ , more than 50% of the  $\delta^{18}O$  variance remains unexplained by a linear fit between  $\delta^{18}O$  and  $T_{SPt}$ . Again we note that this may be an underestimate due to the use of climatological mean boundary conditions.

### 3.3. Forced Warming Temporal Gradients

[45] Using the same linear least square fitting procedure we calculate gradients  $Fa_S^{TIME}$  and  $Fa_{SPt}^{TIME}$  for the forced (F) warming results. These are calculated by fitting a line through the six experiment averages (20-year means). The results in Figure 7 and in Table 4 show that the  $Fa_S^{TIME}$  gradients and correlation coefficients are higher for a forced warming event than for the unforced interannual results. For the forced run results, the regionally averaged results in Table 4 indicate that the forced gradients are very consistent between the different regions:  $Fa_S^{TIME} = 0.36 \pm 0.04$ ‰ °C<sup>-1</sup> and  $Fa_{SPt}^{TIME} = 0.53 \pm 0.03$ ‰ °C<sup>-1</sup> for each of the four regions examined. In general, the ice core site gradients calculated seem to reflect the regional East Antarctic gradients, although Figure 7b shows that over the whole continent  $Fa_S^{TIME}$  can vary between about 0.1 to 0.6‰ °C<sup>-1</sup>. EDML and Dome F  $Fa_S^{TIME}$  values are generally a little larger than the regional values. Dyer tends to reflect the regional Peninsula gradient values quite closely. Byrd has a rather low explained variance (EV) value, which suggests that it is difficult to interpret. Generally however,

**Table 4.** Forced Multiannual Multirun Results for  $a_S^{TIME}$  and  $a_{SPt}^{TIME}$ 

Region	Using Unweighted $T_S$			Using P-Weighted $T_{SPt}$		
	$a$	EV	SIG, %	$a$	EV	SIG, %
<i>Forced Fits Using 20 Years of Each Run</i>						
Antarctic	0.36	0.74	97.1	0.50	0.77	97.9
East Antarctic	0.38	0.82	98.6	0.51	0.86	99.2
West Antarctic	0.37	0.83	98.9	0.56	0.91	99.7
Peninsula	0.32	0.80	98.3	0.54	0.83	98.8
<i>Mean Summer Results (DJF)</i>						
Antarctic	0.37	0.83	98.9	0.40	0.77	98.0
<i>Mean Winter Results (JJA)</i>						
Antarctic	0.72	0.82	98.6	0.69	0.86	99.2
<i>Averaging Radius 200 km (51 × 50 km<sup>2</sup> Grid Points)</i>						
DOME C	0.34	0.72	96.6	0.53	0.95	99.9
EDML	0.60	0.79	98.2	0.85	0.73	96.8
DOME F	0.52	0.82	98.7	0.47	0.95	99.9
BYRD	0.50	0.56	91.3	0.60	0.83	98.8
DYER	0.38	0.75	97.4	0.59	0.79	98.3

<sup>a</sup>Notation:  $a$ , gradient; EV, explained variance ( $R^2$ ); SIG, significance.

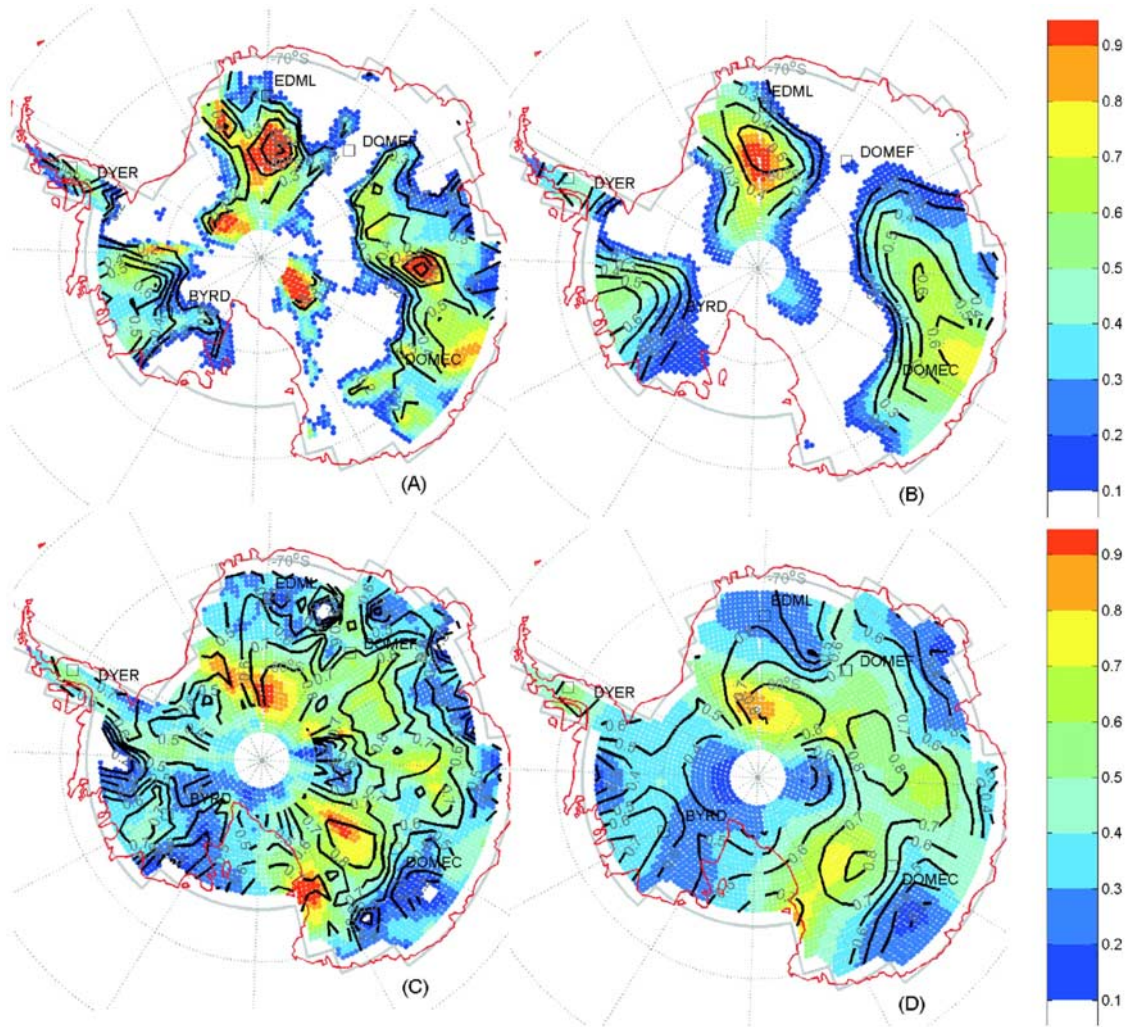


**Figure 6.** Temporal gradients  $UFa_S^{TIME}$  and  $UFa_{SPi}^{TIME}$  for enforced interannual fits (the gradient over 20-year stationary time series of  $\delta^{18}O$  against  $T_S$ ). (a)  $UFa_S^{TIME}$  no spatial averaging and (b)  $UFa_S^{TIME}$  400-km radius averaging. (c)  $UFa_{SPi}^{TIME}$  (using precipitation-weighted temperature against  $T_S$ ) no spatial averaging and (d)  $UFa_{SPi}^{TIME}$  400-km radius averaging. This form of spatial averaging prior to the fitting does not affect the mean Antarctic value of  $UFa_S^{TIME}$  which is  $0.20 \pm 0.005$  for Figures 6a and 6b and  $0.42 \pm 0.005$  for Figures 6c and 6d. The correlation coefficients for the fits are contoured and labeled, using a 0.1 contour interval for Figures 6a and 6b and a 0.2 interval for Figures 6c and 6d.

the EV associated with the forced warming linear fits is high, with less than 20% of the  $\delta^{18}O$  variance left unexplained by the local temperature. This does not leave much room for the fitted gradients to be significantly in error.

[46] Preliminary Last Glacial Maximum (LGM) model runs using HadAM3 (unpublished) indicate that the gradient  $Fa_S^{TIME}$  for the whole continent is for the LGM to PD climate change  $0.92 \pm 0.06 \text{‰ } ^\circ\text{C}^{-1}$  and for the East Antarctic  $Fa_S^{TIME} = 0.74 \pm 0.15 \text{‰ } ^\circ\text{C}^{-1}$ . These results require further experiments and analysis to confirm them, however they agree with previously published LGM to present day model run gradients. *Werner et al.* [2001] calculate  $Fa_S^{TIME} = 0.73 \pm 0.06 \text{‰ } ^\circ\text{C}^{-1}$  for the East Antarctic and  $0.85 \pm 0.07 \text{‰ } ^\circ\text{C}^{-1}$  for the West Antarctic. *Jouzel et al.* [2007] (see their supplements) present a gradient in  $\delta D$  of  $6.2 \text{‰ } ^\circ\text{C}^{-1}$ , which is approximately equivalent to  $Fa_S^{TIME} = 0.75 \text{‰ } ^\circ\text{C}^{-1}$  for  $\delta^{18}O$ . This agreement with previous temporal modeling studies of  $\delta^{18}O$  and

temperature implies that it is unlikely that the low  $Fa_S^{TIME}$  values we calculate over the modeled warming event are specific only to this model.

[47] We note that the gradient for the Dyer site (typical for the Antarctic Peninsula) is  $0.38 \text{‰ } ^\circ\text{C}^{-1}$ . This implies that, for regions that have experienced the warming observed on the western Antarctic Peninsula, represented by the station East Faraday/Vernadsky [*Vaughan et al.*, 2003], of  $2.8^\circ\text{C}$  in the period 1951–2001, then the forced warming gradient would lead us to expect perhaps an increase in  $\delta^{18}O$  of approximately 1‰ to have occurred (if this can be considered a forced warming).

[48] Figure 7 indicates that the central East Antarctic Plateau region tends to have low forced warming  $Fa_S^{TIME}$  values. Note, in particular that the Dome C value of the critical  $Fa_S^{TIME}$  gradient is around  $0.34 \text{‰ } ^\circ\text{C}^{-1}$ , far below the value equivalent to  $0.75 \text{‰ } ^\circ\text{C}^{-1}$  that was used in recent temperature reconstructions [*Jouzel et al.*, 2007]. This

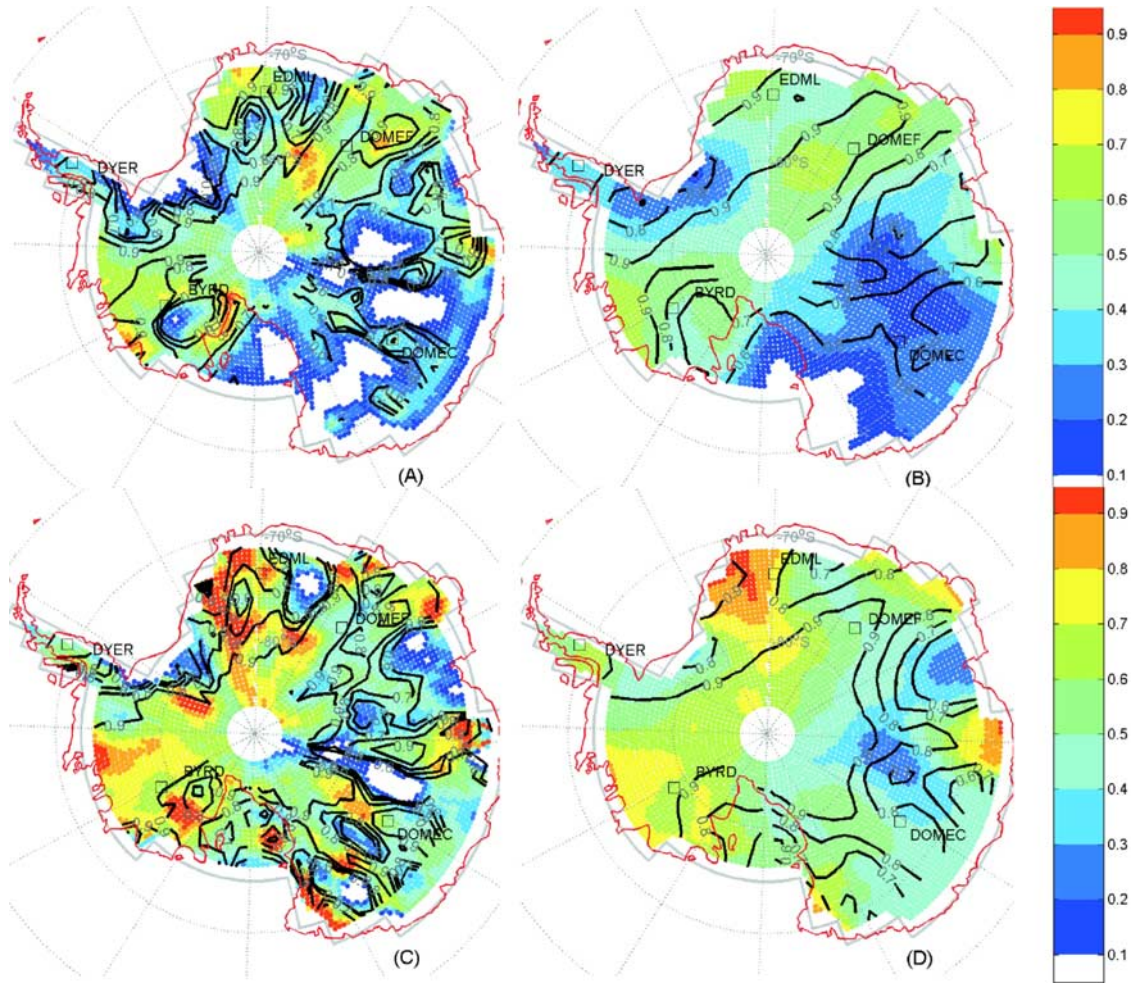


**Figure 7.** Gradients  $Fa_S^{TIME}$  and  $Fa_{SPt}^{TIME}$  for forced 100-year warming fits (the gradient over 100-year warming time series of  $\delta^{18}O$  against  $T_S$ ). (a)  $Fa_S^{TIME}$  no spatial averaging, (b)  $Fa_S^{TIME}$  400-km radius averaging, (c)  $Fa_{SPt}^{TIME}$  no spatial averaging, and (d)  $Fa_{SPt}^{TIME}$  400-km radius averaging. This form of spatial averaging prior to the fitting does not significantly affect the mean Antarctic value of  $Fa_S^{TIME}$  which is  $0.38 \pm 0.005$  for Figures 7a and 7b and  $0.56 \pm 0.005$  for Figures 7c and 7d. The correlation coefficients for the fits is contoured and labeled, using 0.2 contour intervals.

suggests that, near present-day climate conditions, small isotopic changes in the EPICA Dome C region due to GHG change could indicate much larger than expected increases in surface temperature.

### 3.4. Relationship Between Unforced and Forced Temporal Gradients

[49] Owing to the low gradients, correlations, and the confidence intervals shown for  $UFa^{TIME}$  the regional gradients are not significantly different between the unforced and forced temporal gradients. From Figures 6 and 7 it is difficult to find any spatial relationship between the forced warming gradients and the unforced gradients (which are approximately equivalent to those derived using short instrumental records). Figure 8 shows how they directly relate to each other.  $UFa_S^{TIME}$  and  $UFa_{SPt}^{TIME}$  are plotted against  $Fa_S^{TIME}$  and  $Fa_{SPt}^{TIME}$  for locations where the minimum correlation coefficient of the two fits is greater than 0.6 (i.e.,  $T_S$  (Figures 8a and 8b) or  $T_{SPt}$  (Figures 8c and 8d) explains at least 36% of the local temporal  $\delta^{18}O$  variance).

The bunching of the data points by color shows that there is spatial structure in the relationship. Note that some auto correlation is present in all the model output, regardless of spatial averaging. Therefore trails of autocorrelated points appear in all of the Figure 8 panels. But generally, Figure 8 confirms that spatially there is almost no relationship between the short term instrumental type temporal gradients, and forced warming temporal gradients. This reinforces the observational findings, and suggests that it may not be possible to use short-term (2-decade-long)  $\delta^{18}O$  against temperature records to interpret warming events in longer-term ice-core records.

### 3.5. Synoptic Versus Seasonal Precipitation-Weighted Biasing

[50] Table 4 and Figure 7 show that the  $Fa_{SPt}^{TIME}$  gradients are higher than  $Fa_S^{TIME}$  for each region and most core sites (except for Dome F). Figure 9 shows the difference between the gradients. This strong difference between the temporally precipitation-weighted  $Fa_{SPt}^{TIME}$  compared to  $Fa_S^{TIME}$

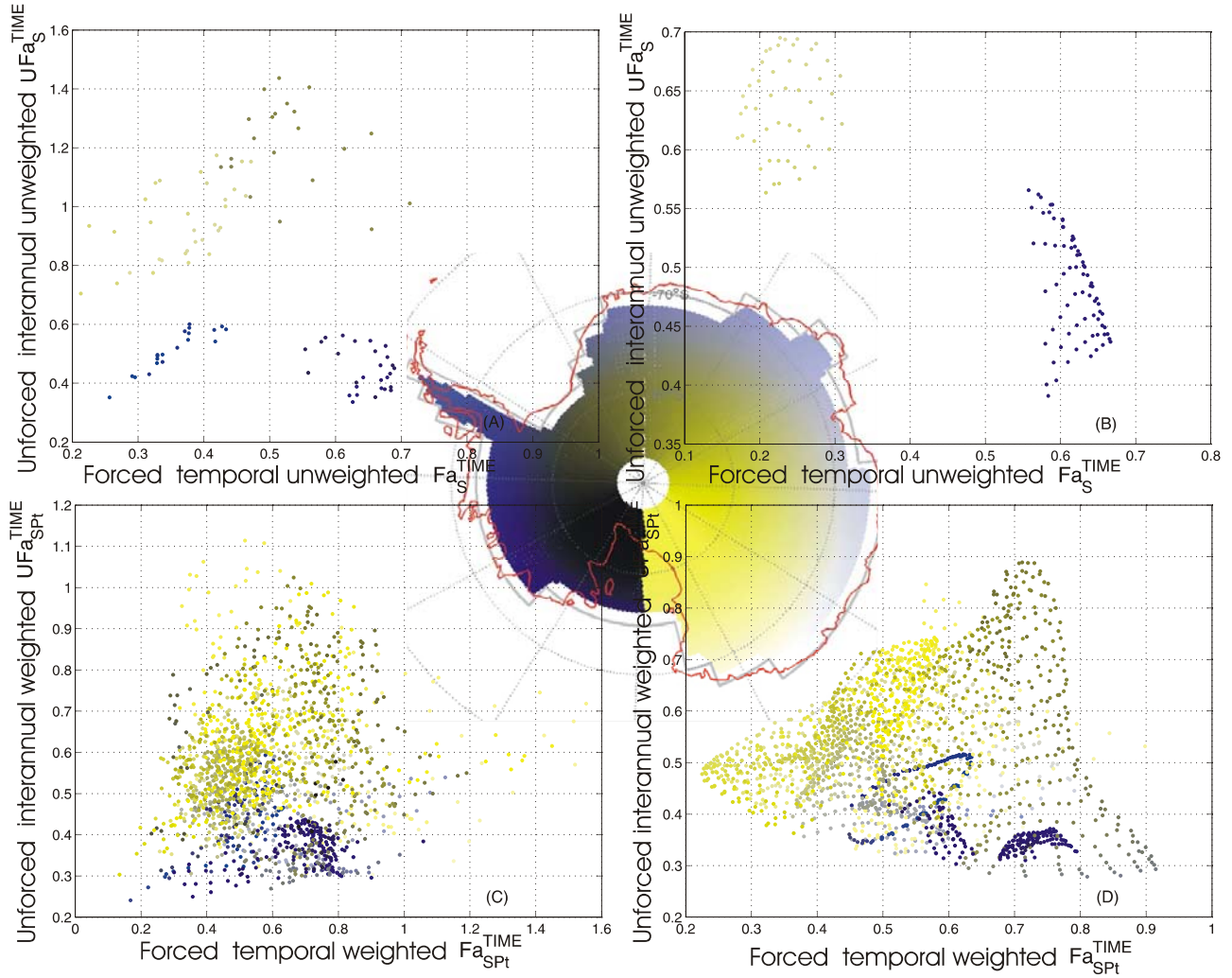


**Figure 8.** Gradients  $UFa_S^{TIME}$  and  $UFa_{SPt}^{TIME}$  against  $Fa_S^{TIME}$  and  $Fa_{SPt}^{TIME}$ . The panels show gradients in Figure 6 against the gradients in Figure 7; that is, the arrangements of panels here is equivalent to those in Figures 6 and 7. The location of each point is colored according to its latitude, longitude, and distance from the coast, as shown in the color location map underneath the panels. (a) Unforced against forced  $a_S^{TIME}$  no spatial averaging, (b) unforced against forced  $a_S^{TIME}$  400 km radius averaging, (c) unforced against forced  $a_{SPt}^{TIME}$  no spatial averaging, and (d) unforced against forced  $a_{SPt}^{TIME}$  400 km radius averaging. Points are only shown if the minimum correlation of the two linear fits is above 0.6, so that the gradients plotted both mean that  $\delta^{18}O$  explains at least 36% of the temperature variance.

indicates that  $B$  is changing over the warming event. For brevity we write the overall change, between the beginning and end of the warming, in  $B$  as

$$\Delta B(x, y) = B_{2100}(x, y) - B_{PD}(x, y), \quad (3)$$

where  $B_{2100}$  is the precipitation-weighted biasing (equation (2)) at each location  $(x, y)$  for the 2100 experiment and  $B_{PD}$  is for the present-day experiment.

[51] In the PD experiment the inland  $B$  varies between +8 and +10°C, see Figure 10a (mean of +9.2°C for East Antarctica; +6.7°C for West Antarctic; and +6.5°C for the more coastal Peninsula). By 2100 this has changed by −0.79°C, −0.79°C and −1.27°C, respectively (see the colored shading on Figure 10a for  $\Delta B$ ). The reduction in  $B$  is almost linear over the simulated warming for each of the

regions (not shown). This means that for the regional results,  $\Delta B$  accounts for almost all the difference in the linear fits between  $Fa_S^{TIME}$  and  $Fa_{SPt}^{TIME}$ ; this is why Figures 9 and 10d are similar. (The  $\Delta B$  changes come out as 26%, 34%, and 41% of  $\Delta T_S$  (where we define  $\Delta T_S$  similarly to equation (3)) for East Antarctica, West Antarctica, and the Peninsula, respectively. This compares with equivalent changes of 25%, 32%, and 45%, in  $(Fa_{SPt}^{TIME} - Fa_S^{TIME})/Fa_{SPt}^{TIME}$  for each of the regions.) Lower  $a_S^{TIME}$  compared to  $a_{SPt}^{TIME}$  indicates that precipitation-weighted  $T_{SPt}$  tends to attenuate temperature changes through time in  $T_S$ . This implies that the changes in  $\delta^{18}O$  related to temperature tend to be smaller than would otherwise be expected.

[52] We can gain insight into why  $B$  changes during the warming event by decomposing  $B$  using bandpass filtering. We obtain frequency filtered  $T_S$  and precipitation  $P$  signals.

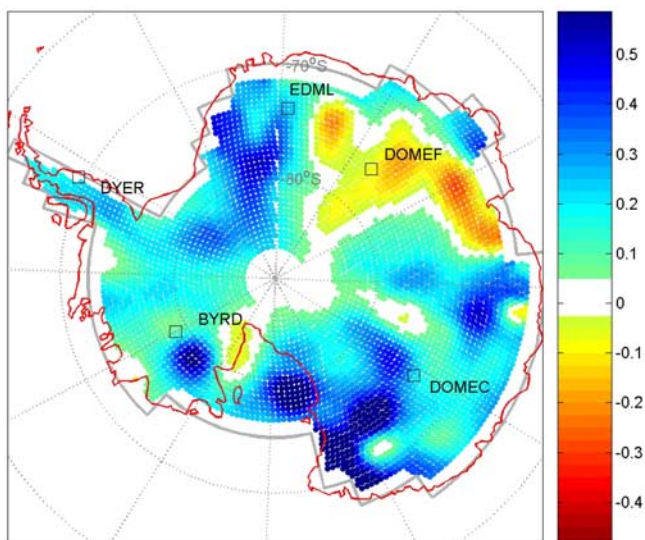


**Figure 9.** Differences in forced run gradient  $F_{a_{SPi}}^{TIME} - F_{a_S}^{TIME}$  over the forced warming using a 200-km spatial averaging radius before the linear fits.

Here we use three frequency bands: high-pass (e.g., high-pass temperature is termed  $T_{HPS}$ ) synoptic (subseasonal) frequencies of <60 days; midpass seasonal frequencies of 61–375 days; and low-pass interannual >375 day frequencies. We then use these band-pass filtered signals of  $T_S$  and  $P$  to generate a frequency decomposed version of  $B$ ,

$$B(x,y) = B^{SYNO}P(x,y) + B^{SEAS}(x,y) + B^{INTER}(x,y), \quad (4)$$

where, like equation (1),

$$B^{SYNO}P(x,y) = \frac{\sum_t (T'_{HPS}(x,y)P'_{HP}(x,y))}{\sum_t P(x,y)}, \quad (5)$$

$T'_{HP}$  is the high-pass filtered synoptic (subseasonal) frequency signal of  $T_S$ . We define  $T'_S$  as  $T_S$  with the time mean  $T_S$  removed.  $T'_{HP}$  is calculated using a standard inverse discrete fast Fourier transform of  $T'_S$ .  $P'_{HP}$  is the equivalent high-pass filtered precipitation signal. Frequency decomposed  $B^{SEAS}$  (seasonal) and  $B^{INTER}$  (interannual) are defined in the same way, using the appropriately frequency filtered signals. Although equation (4) requires  $B^{INTER}$  to fully reconstruct  $B$ , for the model output here,  $B^{INTER}$  is always less than  $|0.5|$  °C, and  $\Delta B^{INTER}$  (changes between PD and 2100) are generally less than  $|0.1|$  °C. Mean

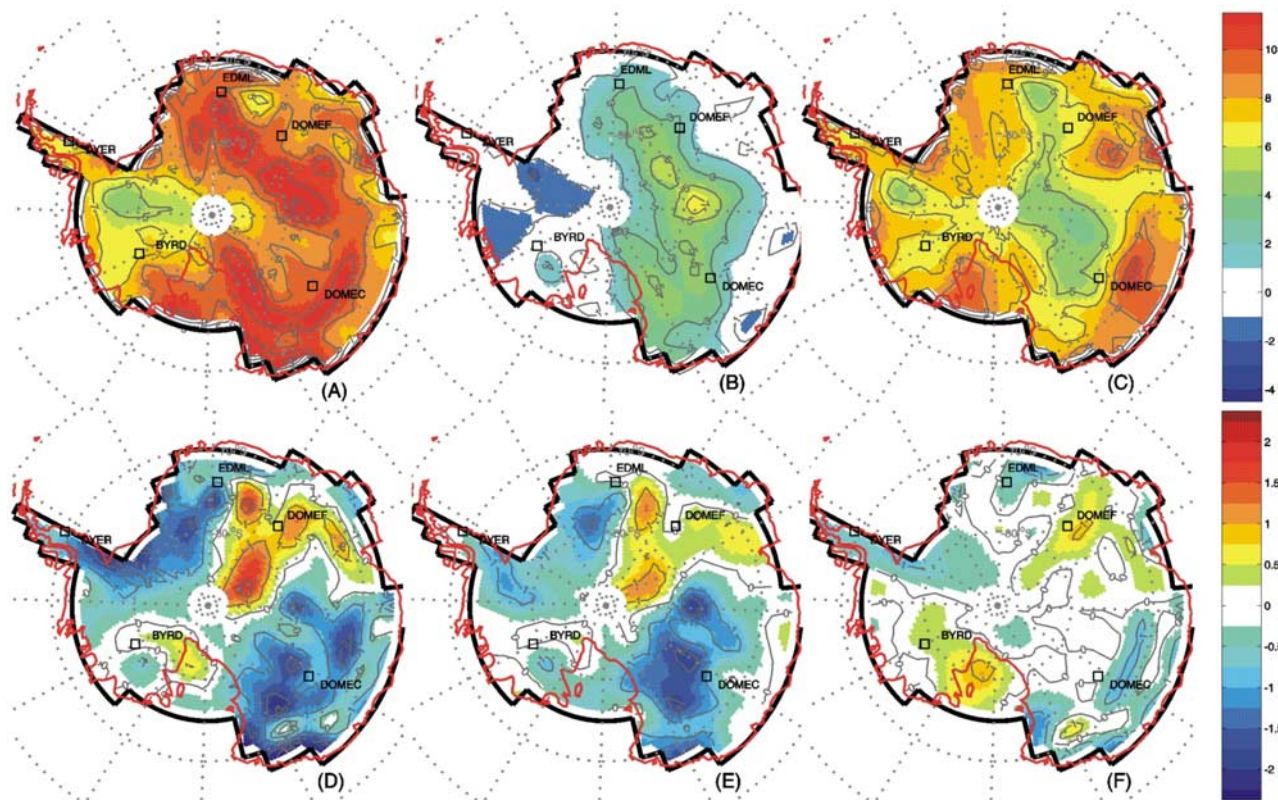


**Figure 10.** Present-day experiment precipitation biasing for (a) total  $B$  (covariance of temperature and precipitation), contoured at 2°C degree intervals; (b) seasonal  $B_{SEAS}$  shaded (60- to 375-day covariance signal); and (c) synoptic  $B_{SYNO}$  (<60-days covariance signal). Figures 10a–10c are on the same color axis.  $\Delta B$  (i.e., the difference in  $B$  between 2100 and the PD) for (d) total  $\Delta B$ , contoured at 1°C degree intervals; (e) seasonal  $\Delta B_{SEAS}$  (60- to 375-day covariance signal); and (f) synoptic  $\Delta B_{SYNO}$  (<60 days covariance signal). All  $B$  and  $\Delta B$  values are calculated using a 200-km equal area averaging radius.

Antarctic  $\Delta B^{INTER}$  is  $-0.07^\circ\text{C}$ ,  $\sigma = 0.12^\circ\text{C}$ . Therefore since  $B^{INTER}$  is very small we omit  $B^{INTER}$  and  $\Delta B^{INTER}$  from the following results. Note however, that for  $\delta^{18}\text{O}$  and  $T$  data time series with more low-frequency climate variability, or example, with El Niño changes [Tindall et al., 2008],  $B^{INTER}$  and  $\Delta B^{INTER}$  may become important.

[53] The results (Figures 9 and 10) indicate that the majority of the present-day biasing  $B$  (Figure 10a) is due to  $B_{SYN}$  (Figure 10c). The synoptic biasing of  $\sim +6^\circ\text{C}$  for the East Antarctic (Figure 10c) is determined by the precipitation regime. It is not clear from observations if a regime that is dominated by clear skies precipitation [Bromwich, 1988] would be liable to substantial subseasonal  $P$  against  $T_S$  covariance. GCMs of the type used here do not specifically parameterize clear-skies precipitation. However, in possible favor of  $B_{SYN} \approx +6^\circ\text{C}$ , winds from lower warmer regions can correlate with  $P$ , so higher-frequency covariance of  $P$  and  $T_S$  seems likely. Bromwich [1988] indicates that for inland East Antarctic precipitation from clouds and clear skies are both generated by the same mechanism of orographic lifting of moist air, so the lack of clear-skies parameterization may not be critical. But, in general, the frequency-magnitude distribution of inland Antarctic precipitation events is not well known, thus it is difficult to further test whether the modeled subseasonal  $B$  and  $\Delta B$  are really representative of the present-day Antarctic or of warmer climate conditions. Further observations of inland  $P$  against  $T_S$  covariance would be useful for testing these  $B_{SYN}$  results.

[54] Interestingly, it is changes in both synoptic covariance  $\Delta B^{SYN}$  (Figure 10f) and the lower-frequency seasonal covariance  $\Delta B^{SEAS}$  (Figure 10e) over warming periods that reduce  $Fa_S^{TIME}$  compared to  $Fa_{SPt}^{TIME}$ , i.e., reducing overall biasing  $B$  over the period of the warming. Where the synoptic biasing difference  $\Delta B^{SYN}$  is negative, this indicates a lesser difference under warmer climate between the temperature under weather systems which carry precipitation and the mean local temperature. The  $B^{SYN}$  changes could be accounted for by changes in the frequency, magnitude, or duration of the synoptic weather systems. We note that synoptic changes seem to be more important around the coastal region, but it is the seasonal changes which are critical and explain most of  $\Delta B$  for the forced warming for inland Antarctica. Negative  $\Delta B^{SEAS}$  is due to the annual precipitation cycle becoming seasonally flatter, or biased toward colder/winter values.

[55] The  $\Delta B^{SEAS}$  (changes in the precipitation seasonality over a warming event) reduce the temporal gradients around the Dome C region (and apparently also near Vostok) from about  $0.53\text{‰}^\circ\text{C}^{-1}$  to about  $0.34\text{‰}^\circ\text{C}^{-1}$ . Although there are also smaller areas where  $\Delta B^{SEAS}$  (and  $\Delta B^{SYN}$  in the more coastal areas) is positive, increasing  $B$  over the warming event.

[56] From the precipitation observations available it is difficult to ascertain if the modeled present-day precipitation seasonality is accurate (see section 2.2.1) but we note first that the geographical distribution of precipitation seasonality in Figure 10b is very similar to the summer precipitation pattern shown by the Helsen et al. [2007] modeling study, secondly we do not seem to be in disagreement with the available observations described in section 2.2.1. Together this provides limited support for the general modeled

reduction of  $Fa_{SPt}^{TIME}$  about  $0.53\text{‰}^\circ\text{C}^{-1}$  to  $Fa_S^{TIME}$  about  $0.34\text{‰}^\circ\text{C}^{-1}$  over the GHG induced warming.

[57] These results are in contrast to the results by studies by Krinner et al. [1997], Delaygue et al. [2000], Werner et al. [2001], and Krinner and Werner [2003]. They find that the glacial-interglacial changes in precipitation seasonality in inland East Antarctic are small. Delaygue et al. [2000] suggest that the seasonality changes over a major cooling give a 15% decrease in  $Fa_{SPt}^{TIME}$  compared to  $Fa_{SA}^{TIME}$ . The results above suggest that for GHG warming events the change could be of the opposite sign and much larger.

#### 4. Conclusions

[58] A gap exists between our understanding of Antarctica's short instrumental and satellite records and isotopic ice core data from Antarctica [Schneider et al., 2004; Monaghan et al., 2006]. It is therefore of considerable interest to investigate how isotopes behave under the conditions expected over the next century.

[59] By introducing an equal area regriding of  $\delta^{18}\text{O}$  and  $T_S$  we show that the East Antarctic spatial gradient  $a_S^{SPACE} = 0.73 \pm 0.08\text{‰}^\circ\text{C}^{-1}$  we model is not statistically different from the observed gradient for the best comparable data from the Masson-Delmotte et al. [2008] observation set. Additionally, our spatial variation  $a_S^{SPACE}$  (using our equal area sampled model output) is similar to that observed both by Masson-Delmotte et al. [2008] and modeled by Helsen et al. [2007] in a present-day backward trajectory model. This gives confidence that the general geographical structure in locally subsampled model  $a_S^{SPACE}$  is robust. We find that the spatial gradients calculated are strongly dependent on the applied subset sampling radius and tend to increase with increasing sampling radii. Likewise the mean correlations obtained for the linear fits are also related to the spatial radius (Figure 5b). While we would expect the correlations, and the gradient to be related (owing to the dependence of the degrees of freedom on radius) this still requires further investigation since it implies that it is difficult to calculate a "representative" local spatial gradient. These systematic sample definition problems may occur, on top of the spatial variation shown by Helsen et al. [2007] and Masson-Delmotte et al. [2008] and here, whenever trying to define a representative local  $a_S^{SPACE}$  value.

[60] The temporal  $\delta^{18}\text{O}$  against  $T_S$  gradients we have calculated here over a  $2.6^\circ\text{C}$  global warming simulation are consistent between different Antarctic regions:  $Fa_S^{TIME} = 0.36 \pm 0.04\text{‰}^\circ\text{C}^{-1}$  for each of the four regions examined (F stands for forced warming), although local EDML and Dome F ice-core site gradients are a little higher. The Dome C and general East Antarctic  $Fa_S^{TIME}$  is about  $0.36 \pm 0.04\text{‰}^\circ\text{C}^{-1}$ , about half the value equivalent to  $0.75\text{‰}^\circ\text{C}^{-1}$  that was used in recent temperature reconstructions [Jouzel et al., 2007]. This suggests that, GHG warmings may leave a smaller than expected imprint on the stable water isotope record across Antarctica. Agreement with previous LGM modeling studies of the  $\delta^{18}\text{O}$  and  $T_S$  relationship suggests that the low  $Fa_S^{TIME}$  values we calculate over the modeled warming event are not specific to HadAM3.

[61] For the forced warming event, decadal averaged  $\delta^{18}\text{O}$  can explain around 75% of the centennial warming variability in  $T_S$ . This compares to unforced climate varia-

tion from short-term (20-year) time series of annually averaged  $\delta^{18}\text{O}$  which typically explain less than 10% of the interannual variability in  $T_S$ . We note that these short-term (20-year) time series are from simulations run with climatological mean SST and sea ice. Therefore they are likely to underestimate the true correlations and gradients between  $\delta^{18}\text{O}$  and  $T_S$ . However, they do provide limited support for the observational findings of low explained variance at Neumayer by *Schlosser and Oerter* [2002] and modeled results by *Werner and Heimann* [2002]. There is little agreement between  $\delta^{18}\text{O}$  against  $T_S$  gradients for the forced warming and those from short unforced (climatological mean driven) 20-year interannual time series for any particular Antarctic regions or locations. This would agree with these previous authors who have highlighted the difficulties in trying to use short-term isotope-temperature records to aid in the interpretation of longer-term ice-core records.

[62] The precipitation-weighted gradient, for the warming event, is larger (at  $Fa_{SPt}^{TIME} = 0.53 \pm 0.03\text{‰ } ^\circ\text{C}^{-1}$ ) than the standard gradient ( $Fa_S^{TIME}$ ) using surface temperature for the regions examined. For the CO<sub>2</sub> warming event modeled here  $Fa_{SPt}^{TIME}$  is 40–50% larger than  $Fa_S^{TIME}$  for the East Antarctic and Dome C. This is in contrast to modeling study results by *Krinner et al.* [1997]; *Delaygue et al.* [2000]; *Werner et al.* [2001] who note that the glacial-interglacial changes in precipitation seasonality are small for the Antarctic. To investigate this, we have introduced a frequency decomposition of the local influence on  $\delta^{18}\text{O}$ . This decomposition, using bandpass filtering, shows that the majority of the present-day biasing  $B$  is due to synoptic (between 1 and 60 day) frequency variations in the covariance in  $T_S$  and  $P$ , but a significant proportion in the East Antarctic plateau region is due to seasonal covariance. Over the warming event simulated this biasing tends to reduce across most of Antarctica. The reduction in  $Fa_S^{TIME}$  (at  $0.36 \pm 0.04\text{‰ } ^\circ\text{C}^{-1}$ ) compared to the precipitation-weighted temperature  $Fa_{SPt}^{TIME}$  (at  $0.50 \pm 0.03\text{‰ } ^\circ\text{C}^{-1}$ ) is mainly due to changes in the seasonal covariance part of  $B$ ; especially inland in the East Antarctic region. However, changes in the synoptic frequencies have some effect on the spatial pattern of  $B$ , particularly in the more coastal regions. The zonal changes in precipitation may be related to changes in the circumpolar low-pressure trough influencing the mean cyclone track [*Bromwich*, 1988], further investigation of which is merited.

[63] This study has not addressed other important processes which might be affecting the forced warming gradients. In particular, the model is not currently set up to enable the tracking of water vapor sources, thus we do not know if changes in the temperature of source regions may also be impacting the temporal  $\delta^{18}\text{O} - T_S$  gradients, and/or changes in atmospheric overturning circulation [*Noone*, 2008]. We note that experiment boundary conditions include some sea surface temperature warming at all latitudes, so if the source region remained unchanged then the difference in source and site temperature would be significantly less than the change in site temperature. Additionally, we have not looked for systematic changes in condensation (inversion) temperatures (although the model inversion structure for the present day is reasonable). Source temperature and condensation temperature changes could both contribute to the

value of  $Fa_{SPt}^{TIME} = 0.53 \pm 0.03\text{‰ } ^\circ\text{C}^{-1}$  being lower than equivalent LGM to present-day gradients. Without source tracking, it is difficult to determine source temperature, and space constraints preclude a detailed investigation of condensation temperature changes here.

[64] There could be implications from these results for detection of warming trends across all of Antarctica. Our results raise the possibility that the commonly used gradients may not be appropriate for all the climate changes observed in the ice core record of past Antarctic climate. Until now, the isotopic experiments have been carried out for the coldest periods in the record, but further study of the different warm periods is clearly warranted.

[65] **Acknowledgments.** We acknowledge NERC RAPID ISOMAP for funding the model development; *Masson-Delmotte et al.* [2008] for their unpublished manuscript; the modeling groups, the Program for Climate Model Diagnosis and Intercomparison (PCMDI), and the WCRP's Working Group on Coupled Modelling (WGCM) for their roles in making available the WCRP CMIP3 multimodel data set; and three thorough and helpful anonymous reviewers.

## References

- Arthern, R. J., D. P. Winebrenner, and D. G. Vaughan (2006), Antarctic snow accumulation mapped using polarization of 4.3-cm wavelength microwave emission, *J. Geophys. Res.*, *111*, D06107, doi:10.1029/2004JD005667.
- Bracegirdle, T. J., W. M. Connolley, and J. Turner (2008), Antarctic climate change over the twenty-first century, *J. Geophys. Res.*, *113*, D03103, doi:10.1029/2007JD008933.
- Bromwich, D. (1988), Snowfall in high southern latitudes, *Rev. Geophys.*, *26*, 149–168.
- Caillon, N., J. P. Severinghaus, J.-M. Barnola, J. Chappellaz, J. Jouzel, and F. Parrenin (2001), Estimation of temperature change and of gas age–ice age difference, 108 kyr B.P., at Vostok, Antarctica, *J. Geophys. Res.*, *106*, 31,893–31,902.
- Connolley, W. M. (1996), The Antarctic temperature inversion, *Int. J. Climatol.*, *16*, 1333–1342.
- Connolley, W. M., and T. J. Bracegirdle (2007), An Antarctic assessment of IPCC AR4 coupled models, *Geophys. Res. Lett.*, *34*, L22505, doi:10.1029/2007GL031648.
- Cuffey, K., G. Clow, R. Alley, M. Stuiver, E. Waddington, and R. Saltus (1995), Large Arctic temperature change at the Wisconsin-Holocene glacial transition, *Science*, *270*, 455–458.
- Dansgaard, W. (1964), Stable isotopes in precipitation, *Tellus*, *16*, 436–468.
- Dansgaard, W., S. J. Johnsen, N. Reeh, N. Gundestrup, H. B. Clausen, and C. U. Hammer (1975), Climatic changes, Norsemen and modern man, *Nature*, *255*, 24–28, doi:10.1038/255024a0.
- Delaygue, G., J. Jouzel, V. Masson, R. D. Koster, and E. Bard (2000), Validity of the isotopic thermometer in central Antarctica: Limited impact of glacial precipitation seasonality and moisture origin, *Geophys. Res. Lett.*, *27*, 2677–2680.
- Ekaykin, A., V. Lipenkov, N. Barkov, J. Petit, and V. Masson-Delmotte (2002), Spatial and temporal variability in isotope composition of recent snow in the vicinity of Vostok station: Implications for ice-core record interpretation, *Ann. Glaciol.*, *35*, 181–186.
- EPICA Community Members (2004), Eight glacial cycles from an Antarctic ice core, *Nature*, *429*, 623–628, doi:10.1038/nature02599.
- Fawcett, P. J., A. M. Agustsdóttir, R. B. Alley, and C. A. Shuman (1997), The Younger Dryas termination and North Atlantic Deep Water formation: Insights from climate model simulations and Greenland ice cores, *Paleoceanography*, *12*, 23–38.
- Fujita, K., and O. Abe (2006), Stable isotopes in daily precipitation at Dome Fuji, East Antarctica, *Geophys. Res. Lett.*, *33*, L18503, doi:10.1029/2006GL026936.
- Gordon, C., C. Cooper, C. A. Senior, H. Banks, J. M. Gregory, T. C. Johns, J. F. B. Mitchell, and R. A. Wood (2000), The simulation of SST, sea ice extents and ocean heat transports in a version of the Hadley Centre coupled model without flux adjustments, *Clim. Dyn.*, *16*, 147–168.
- Helsen, M., R. van de Wal, and M. van den Broeke (2007), The isotopic composition of present-day Antarctic snow in a Lagrangian atmospheric simulation, *J. Clim.*, *20*, 739–756.
- Hoffmann, G., and M. Heimann (1997), Water isotope modeling in the Asian monsoon region, *Quat. Int.*, *37*, 115–128.

- Hoffmann, G., M. Werner, and M. Heimann (1998), Water isotope module of the ECHAM atmospheric general circulation model: A study on time-scales from days to several years, *J. Geophys. Res.*, *103*, 16,871–16,896.
- Intergovernmental Panel on Climate Change (2007), *Climate Change 2007: The Physical Science Basis. Contribution of Working Group I to the Fourth Assessment Report of the Intergovernmental Panel on Climate Change*, edited by S. Solomon et al., Cambridge Univ. Press, Cambridge, U.K.
- Jouzel, J., C. Lorius, J. R. Petit, C. Genthon, N. I. Barkov, V. M. Kotlyakov, and V. M. Petrov (1987), Vostok ice core: a continuous isotope temperature record over the last climatic cycle (160,000 years), *Nature*, *329*, 403–408, doi:10.1038/329403a0.
- Jouzel, J., R. D. Koster, R. J. Suozzo, and G. L. Russell (1994), Stable water isotope behavior during the Last Glacial Maximum: A general circulation model analysis, *J. Geophys. Res.*, *99*, 25,791–25,802.
- Jouzel, J., et al. (1997), Validity of the temperature reconstruction from water isotopes in ice cores, *J. Geophys. Res.*, *102*, 26,471–26,487.
- Jouzel, J., F. Vimeux, N. Caillon, G. Delaygue, G. Hoffmann, V. Masson-Delmotte, and F. Parrenin (2003), Magnitude of isotope/temperature scaling for interpretation of central Antarctic ice cores, *J. Geophys. Res.*, *108*(D12), 4361, doi:10.1029/2002JD002677.
- Jouzel, J., et al. (2007), Orbital and millennial Antarctic climate variability over the past 800,000 years, *Science*, *317*, 793–796.
- Kohn, M., and J. Welker (2005), Precipitation  $\delta^{18}\text{O}$ -temperature relations: A reexamination, *Earth Planet. Sci. Lett.*, *231*, 87–96.
- Krinner, G., and M. Werner (2003), Impact of precipitation seasonality changes on isotopic signals in polar ice cores: A multi-model analysis, *Earth Planet. Sci. Lett.*, *4*, 525–538.
- Krinner, G., C. Genthon, and J. Jouzel (1997), GCM analysis of local influences on ice core  $\delta$  signals, *Geophys. Res. Lett.*, *24*, 2825–2828.
- Krinner, G., B. Guicherd, K. Ox, C. Genthon, and O. Magand (2008), Influence of oceanic boundary conditions in simulations of Antarctic climate and surface mass balance change during the coming century, *J. Clim.*, *21*, 938–962.
- Lachlan-Cope, T. A., and W. M. Connolley (2006), Teleconnections between the tropical Pacific and the Amundsen-Bellinghousens Sea: Role of the El Niño/Southern Oscillation, *J. Geophys. Res.*, *111*, D23101, doi:10.1029/2005JD006386.
- Lorius, C., and L. Merlivat (1977), Distribution of mean surface stable isotope values in East Antarctica: Observed changes with depth in the coastal area, in *Isotopes and Impurities Snow and Ice, IAHS Publ. 118*, pp. 127–137, Int. Assoc. of Hydrol. Sci., Gentbrugge, Belgium.
- Lorius, C., J. Jouzel, C. Ritz, L. Merlivat, N. I. Barkov, Y. S. Korotkevich, and V. M. Kotlyakov (1985), A 150,000-year climatic record from Antarctic ice, *Nature*, *316*, 591–596, doi:10.1038/316591a0.
- Manabe, S., R. J. Stouffer, M. J. Spelman, and K. Bryan (1991), Transient responses of a coupled ocean-atmosphere model to gradual changes of atmospheric CO<sub>2</sub>. Part I: Annual mean response, *J. Clim.*, *4*, 785–818.
- Marshall, G. (2008), On the annual and semi-annual cycles of precipitation across Antarctica, *Int. J. Climatol.*, in press.
- Masson-Delmotte, V., et al. (2008), A review of Antarctic surface snow isotopic composition: Observations, atmospheric circulation and isotopic modelling, *J. Clim.*, *21*, 3359–3387, doi:10.1175/2007JCLI2139.1.
- Mathieu, R., D. Pollard, J. E. Cole, J. W. C. White, R. S. Webb, and S. L. Thompson (2002), Simulation of stable water isotope variations by the GENESIS GCM for modern conditions, *J. Geophys. Res.*, *107*(D4), 4037, doi:10.1029/2001JD900255.
- Monaghan, A. J., et al. (2006), Insignificant change in Antarctic snowfall since the International Geophysical Year, *Science*, *313*, 827–831.
- Noone, D. (2008), The influence of midlatitude and tropical overturning circulation on the isotopic composition of atmospheric water vapor and Antarctic precipitation, *J. Geophys. Res.*, *113*, D04102, doi:10.1029/2007JD008892.
- Noone, D., and I. Simmonds (2002), Associations between  $\delta^{18}\text{O}$  of water and climate parameters in a simulation of atmospheric circulation for 1979–95, *J. Clim.*, *15*, 3150–3169.
- Parrenin, F., J. Jouzel, C. Waelbroeck, C. Ritz, and J. Barnola (2001), Dating the Vostok ice core by an inverse method, *J. Geophys. Res.*, *106*, 31,837–31,852.
- Paul, A., and C. Schäfer-Neth (2003), Modeling the water masses of the Atlantic Ocean at the Last Glacial Maximum, *Paleoceanography*, *18*(3), 1058, doi:10.1029/2002PA000783.
- Petit, J. R., et al. (1999), Climate and atmospheric history of the past 420,000 years from the Vostok ice core, Antarctica, *Nature*, *399*, 429–436, doi:10.1038/20859.
- Pope, V. D., M. L. Gallani, P. R. Rowntree, and R. A. Stratton (2000), The impact of new physical parametrizations in the Hadley Centre climate model: HadAM3, *Clim. Dyn.*, *16*, 123–146.
- Rayner, N. A., D. E. Parker, E. B. Horton, C. K. Folland, L. V. Alexander, D. P. Rowell, E. C. Kent, and A. Kaplan (2003), Global analyses of sea surface temperature, sea ice, and night marine air temperature since the late nineteenth century, *J. Geophys. Res.*, *108*(D14), 4407, doi:10.1029/2002JD002670.
- Robin, G. D. Q. (1983), Isotopic temperature ( $d - q$ ) noise, in *The Climatic Record in Polar Ice Sheets*, pp. 184–189, Cambridge Univ. Press, New York.
- Rozanski, K., L. Araguas-Araguas, and R. Gonfiantini (1992), Relation between long-term trends of oxygen-18 isotope composition of precipitation and climate, *Science*, *258*, 981–985.
- Salamatin, A. N., V. Y. Lipenkov, N. I. Barkov, J. Jouzel, J. R. Petit, and D. Raynaud (1998), Ice core age dating and paleothermometer calibration based on isotope and temperature profiles from deep boreholes at Vostok Station (East Antarctica), *J. Geophys. Res.*, *103*, 8963–8978.
- Schlusser, E., and H. Oerter (2002), Seasonal variations of accumulation and the isotope record in ice cores—A study with surface snow samples and firn cores from Neumayer Station, Antarctica, *Ann. Glaciol.*, *35*, 97–101.
- Schmidt, G. A., A. N. LeGrande, and G. Hoffmann (2007), Water isotope expressions of intrinsic and forced variability in a coupled ocean-atmosphere model, *J. Geophys. Res.*, *112*, D10103, doi:10.1029/2006JD007781.
- Schneider, D. P., and D. C. Noone (2007), Spatial covariance of water isotopes in ice cores during 20th century climate change, *J. Geophys. Res.*, *112*, D18105, doi:10.1029/2007JD008652.
- Schneider, D. P., E. J. Steig, and J. C. Comiso (2004), Recent climate variability in Antarctica from satellite-derived temperature data, *J. Clim.*, *17*, 1569–1583.
- Schneider, D. P., E. J. Steig, T. D. van Ommen, D. A. Dixon, P. A. Mayewski, J. M. Jones, and C. M. Bitz (2006), Antarctic temperatures over the past two centuries from ice cores, *Geophys. Res. Lett.*, *33*, L16707, doi:10.1029/2006GL027057.
- Schwander, J., J. Jouzel, C. U. Hammer, J.-R. Petit, R. Udisti, and E. Wolff (2001), A tentative chronology for the EPICA Dome Concordia ice core, *Geophys. Res. Lett.*, *28*, 4243–4246.
- Stenni, B., V. Masson-Delmotte, S. Johnsen, J. Jouzel, A. Longinelli, E. Monnin, R. Rothlisberger, and E. Selmo (2001), An oceanic cold reversal during the last deglaciation, *Science*, *293*, 2074–2077.
- Tindall, J., P. Valdes, and L. Sime (2008), Stable water isotopes in HadCM3: The isotopic signature of ENSO and the tropical amount effect, *J. Geophys. Res.*, doi:10.1029/2008JD010825, in press.
- Turner, J., W. Connolley, S. Leonard, G. Marshall, and D. Vaughan (1999), Spatial and temporal variability of net snow accumulation over the Antarctic from ECMWF re-analysis project data, *Int. J. Climatol.*, *19*, 697–724.
- Turner, J., W. M. Connolley, T. A. Lachlan-Cope, and G. J. Marshall (2006), The performance of the Hadley Centre Climate Model (HadCM3) in high southern latitudes, *Int. J. Climatol.*, *26*, 91–112, 10.1002/joc.1260.
- Vaughan, D., G. Marshall, W. Connolley, C. Parkinson, R. Mulvaney, D. Hodgson, J. King, C. Pudsey, and J. Turner (2003), Recent rapid regional climate warming on the Antarctic Peninsula, *Clim. Change*, *60*, 243–274.
- Werner, M., and M. Heimann (2002), Modeling interannual variability of water isotopes in Greenland and Antarctica, *J. Geophys. Res.*, *107*(D1), 4001, doi:10.1029/2001JD900253.
- Werner, M., U. Mikolajewicz, M. Heimann, and G. Hoffmann (2000), Borehole versus isotope temperatures on Greenland: Seasonality does matter, *Geophys. Res. Lett.*, *27*, 723–726.
- Werner, M., M. Heimann, and G. Hoffmann (2001), Isotopic composition and origin of polar precipitation in present and glacial climate simulations, *Tellus, Ser. B*, *53*, 53–71.

W. M. Connolley, L. C. Sime, and E. W. Wolff, British Antarctic Survey, Cambridge CB3 0ET, UK. (lsim@bas.ac.uk)  
 J. C. Tindall and P. J. Valdes, School of Geographical Sciences, University of Bristol, University Road, Bristol BS8 1SS, UK.